ARTICLE

Ultrapotassic plutons as a source of uranium of vein-type U-deposits (Moldanubian Zone, Bohemian Massif): insights from SIMS uraninite U–Pb dating and trace element geochemistry

Martin Kubeš[1,2] · Jaromír Leichmann[1] · Vojtěch Wertich[1,2] · Renata Čopjaková[1] · Markéta Holá[3] · Radek Škoda[1] · Bohdan Kříbek[2] · Julien Mercadier[4] · Michel Cuney[4] · Etienne Deloule[4] · Andreï Lecomte[4] · Ewa Krzemińska[5]

Abstract

The Bohemian Massif hosts significant hydrothermal U-deposits associated with shear zones in the high-grade metamorphic basement. But there is a lack of evidence of a genetic link between mineralization and U-fertile igneous rocks. This contribution provides constraints on the major U source of the vein-type U-deposits, the timing of ore formation and the metallogenetic model. The anomalous trace element signatures of the low-temperature hydrothermal deposits (high Zr, Y, Nb, Ti, $\sum$REE) and their close spatial relation with ultrapotassic rocks of the durbachite series point to a HFSE and REE enriched source rock. The durbachites have high U content (13.4–21.5 ppm) mainly stored in magmatic uraninite and other refractory minerals (e.g., thorite, zircon, allanite) that became metamict over a time interval sufficient to release U from their crystal structure, as suggested by the time gap between emplacement of the durbachites (EMP uraninite U–Pb age ~ 338 Ma) and hydrothermal activity (SIMS uranium ore U–Pb age ~ 270 Ma). Airborne radiometric data show highly variable Th/U ratios (1.5–6.0), likely reflecting a combination between (1) crystallization of magmatic uraninite, (2) hydrothermal alteration, and (3) leaching and mobilization of U along NW–SE-trending fault zones, manifested by elevated Th/U values in the radiometric map. The presence of rare magmatic uraninite in durbachites suggests almost complete uraninite dissolution; EMP imaging coupled with LA-ICP-MS analyses of refractory accessory phases revealed extensive mobilization of U together with HFSE and REE, providing direct evidence for metal leaching via fluid-driven alteration of radiation-damaged U-rich minerals. The large-scale HFSE and REE mobilization, demonstrated by the unusual trace element signatures of the U-deposits, was likely caused by low-temperature (270–300 °C), highly alkaline aqueous solutions containing F-, P-, and K-dominated complexing ligands. The first SIMS U–Pb age of 270.8 ± 7.5 Ma obtained so far for U-mineralization from the Bohemian Massif revealed a main Permian U mineralizing event, related to crustal extension, exhumation of the crystalline basement, and basin formation, as recorded by U–Pb apatite dates (280–290 Ma) and AFT thermal history models of the durbachites. The Permo-Carboniferous sedimentary cover probably represented a source of oxidized basinal brines infiltrating the basement-hosted durbachite plutons and triggering massive metal leaching. The interaction between basin-derived brines and durbachites resulted in significant modification of the chemical composition of the hydrothermal system (K and F release during biotite chloritization, P liberation through monazite alteration), leading to the formation of ore-bearing fluids responsible for the metallogenesis of the basement-hosted unconformity-related U-deposits in shear zones in the Bohemian Massif.

Editorial handling: M. Fayek/P. Ledru

✉ Martin Kubeš
kubes@mail.muni.cz

1 Department of Geological Sciences, Masaryk University, Kotlářská 2, 611 37 Brno, Czech Republic

2 Czech Geological Survey, Klárov 3, 118 21 Prague, Czech Republic

3 Department of Chemistry, Masaryk University, Kamenice, 753/5, 625 00 Brno, Czech Republic

4 Université de Lorraine, CNRS, CREGU, 54500 GéoRessources, Nancy, France

5 Polish Geological Institute – National Research Institute (PGI-NRI), Rakowiecka 4, 00-975 Warsaw, Poland

Introduction

Within the Central and Western European Variscides, a large proportion of uranium (U) mineralization is associated with hydrothermal vein-type U-deposits related to Late-Carboniferous U-fertile peraluminous granites (Romer and Cuney 2018; references therein). It is generally accepted that the U leaching from large volumes of peraluminous leucogranites was triggered by infiltration of meteoric- and basin-derived oxidizing fluids during Permian brittle deformation (ca. 290–260 Ma) (Ballouard et al. 2018; Cathelineau et al. 1990; Marignac and Cuney 1999). Due to the high abundance of primary magmatic uraninite, which controls the whole-rock U budget of the host rocks and represents an easily leachable phase during oxidizing fluid circulation, the leucocratic granites account for a suitable source for the formation of hydrothermal U-deposits (e.g., Bonnetti et al. 2022; Cuney 2014). Accordingly, the nature of U host minerals determines whether the source rock is U-fertile and enables U remobilization by leaching during fluid-rock interaction (Cuney 2009). Refractory accessory phases (e.g., zircon, U-rich thorite, allanite) may also represent potential sources of U and other metals, such as high field strength elements (HFSE; Zr, Hf, Nb, Th) and rare earth elements (REEs), only if they become metamict due to the accumulation of self-induced radiation damage over a time interval sufficient to liberate metals from their crystal structure (Bonnetti et al. 2017; Zhang et al. 2022). Therefore, the radiation damage of accessory phases followed by late fluid-driven alteration may release sufficient amounts of metals, leading to the formation of world-class ore deposits such as hydrothermal U-deposits (McGloin et al. 2015), unconformity-related heavy-REE deposits (Walsh and Spandler 2023), granite-hosted polymetallic Zr-REE-Nb–Ta deposits (Yang et al. 2014; Zeng and Liu 2022), and ion-adsorption REE deposits (Zhang et al. 2023). In this context, the characterization of main accessory phases in ore-fertile granitic rocks, combined with the trace element geochemistry and age dating of ore deposits, can provide crucial constraints on their mutual metallogenetic link (Mercadier et al. 2011a; Bonnetti et al. 2018). Besides, other important factors governing the leaching process and fluid migration (e.g., ligand activity, fault systems, heat production) must be considered to provide complex insight into the ore deposit formation (e.g., Ballouard et al. 2017; Cuney and Kyser 2015; Hasterok et al. 2018; Kříbek et al. 2009).

In the Moldanubian Zone of the Bohemian Massif, which hosts economically significant U-deposits associated with brittle shear zones in high-grade metamorphic complexes (Kříbek et al. 2009) similar to other Variscan U-deposits (e.g., Cuney et al. 1990; Hofmann and Eikenberg 1991; Velichkin and Vlasov 2011), there is a lack of evidence of the spatial relation of the vein-type U-mineralization to U-fertile granitic rocks, thus the potential U-source remains a matter of debate. Furthermore, due to the absence of precise geochronological data, their metallogenetic model and timing in the larger frame of the Central European Variscides are poorly constrained.
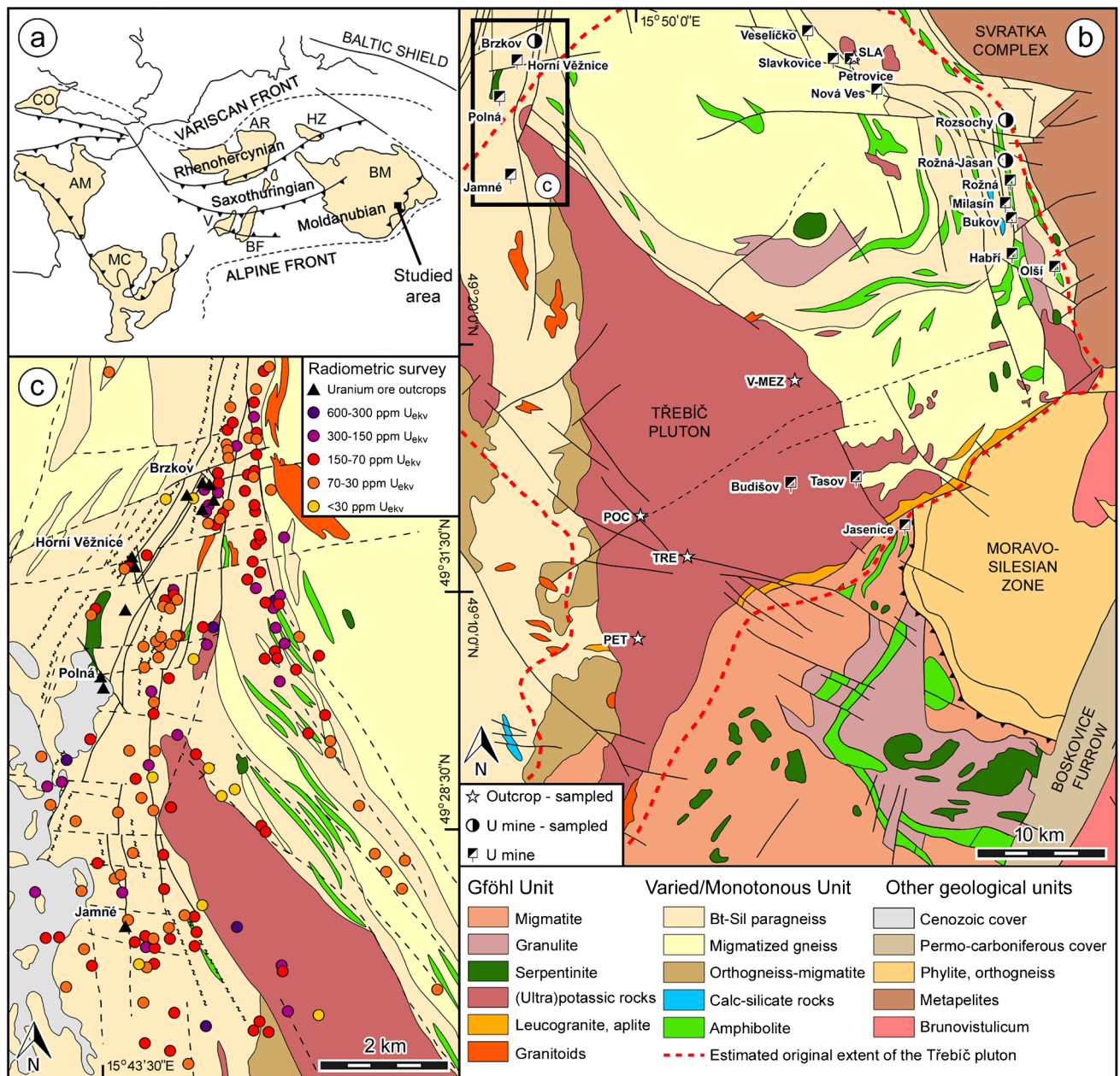
In this study, we present new mineralogical, geochemical, thermochronological, and geochronological data obtained for ultrapotassic plutons (durbachites) and U-deposits (vein-type mineralization) to decipher the main U-source of these ore deposits belonging to the Western Moravian U-province from the Moldanubian Zone of the Bohemian Massif (Fig. 1a, b). The unusual trace element signatures of the studied U-deposits mimicking those of common accessory phases in ultrapotassic rocks, which experienced the extensive fluid-driven alteration responsible for massive HFSE and REE remobilization, point towards their possible genetic relation. The results have important implications for understanding the potential metal sources, micro- to large-scale metal leaching, transport pathways, and compositions of aqueous solutions responsible for the metallogenesis of hydrothermal vein-type U-deposits. Moreover, we present the first in-situ geochronological U–Pb age obtained so far for the U-mineralization from the Bohemian Massif, providing constraints on a metallogenetic model of the Moldanubian U-deposits and timing of their formation in the frame of the European Variscan belt.

Geological background

The Moldanubian Zone of the Bohemian Massif

The Western Moravian U-province is situated in the eastern part of the Moldanubian Zone of the Bohemian Massif (Fig. 1a–c) that represents the high-grade Variscan orogenic root in Central Europe. This internal orogenic domain mostly consists of medium- to high-grade metamorphic rocks extensively intruded by numerous granitic plutons (Žák et al. 2014).

The Moldanubian Zone is traditionally subdivided into two principal tectonostratigraphic units having different lithological assemblages and metamorphic conditions: the Monotonous, Varied and Gföhl Units (e.g., Lardeaux et al. 2014; Matte et al. 1990). Mid-crustal, amphibole-facies Monotonous and Varied Units are mainly composed of migmatitic cordierite-biotite-sillimanite paragneisses along with minor orthogneisses and amphibolites; abundant intercalations of calcsilicate rocks, marble, quartzite, and graphitic gneiss are only typical of the Varied Unit. Minor spinel-bearing peridotites and retrogressed eclogites are present as

Fig. 1 a Location of the Bohemian Massif and occurrences of the Variscan basement within the regional frame of western-central Europe. **b** Simplified geological map of the eastern Moldanubian Zone hosting numerous hydrothermal vein-type U-deposits and widespread ultrapotassic intrusions of the durbachite series. The red dashed line displays the original extent of durbachite intrusions estimated based on geophysical and petrological data (Leichmann et al. 2017). The highlighted location of the Brzkov deposit and other U ore outcrops is enlarged in **c**, detailed geological map showing a close spatial relation between the Třebíč durbachite pluton and the Brzkov deposit along with U-mineralization recorded by borehole logging and surface radiometric survey (radiometric anomalies in a range <30–600 ppm U_{ekv}; data from Ondřík 1998). Individual maps modified on the basis of the Czech Geological Survey online maps application (https://www.geology.cz). Sampling localities of durbachites: TRE=Třebíč, V-MEZ=Velké Meziříčí, SLA=Slavkovice, POC=Pocoucov, PET=Petrůvky

well. The lower crustal Gföhl Unit, which is found structurally on the top of the Moldanubian sequence, represents a subduction-related tectonic mélange predominantly formed by anatectic orthogneisses and amphibolites along with abundant felsic granulite bodies (Cooke and O'Brien 2001;

Tajčmanová et al. 2006) closely associated with tectonic lenses of spinel- and garnet-bearing peridotites with eclogite and pyroxenite layers (Kubeš et al. 2022a). Neoproterozoic-Early Paleozoic sedimentation ages were determined for the protolith of Monotonous and Varied assemblages

(Košler et al. 2014). By contrast, the magmatic protolith of the Gföhl gneisses shows Cambrian-Devonian ages (Friedl et al. 2004).

Overthrusting of the Gföhl Unit over the less allochthonous Monotonous and Varied Units resulted in widespread metamorphism, with a peak stage at ~ 340 Ma (O'Brien and Rötzler 2003), and was concurrently accompanied by extensive plutonic activity occurring in contrasting geodynamic settings (from subduction zone environment to post-orogenic uplift and extension), mostly from the Late Devonian to the Carboniferous (e.g., Finger et al. 1997; Timmerman 2008; Žák et al. 2014). These various igneous stages include (1) calc-alkaline and high-K calc-alkaline subduction-related suites of the Central Bohemian Plutonic Complex (~ 373–340 Ma); (2) ultrapotassic plutons belonging to so-called durbachite series (ultrapotassic biotite-amphibole melasyenites with conspicuous K-feldspar phenocrysts), associated with rapid exhumation of the Gföhl Unit to mid-crustal assemblages (~ 335–355 Ma); (3) peraluminous anatectic S-type granitoids (~ 330–326 Ma) followed by (4) calc-alkaline intrusions with I-type affinity of the Moldanubian Plutonic Complex (~ 320–300 Ma). The vigorous ultrapotassic magmatism of the Moldanubian Zone, a characteristic feature of the entire Variscan Orogenic Belt in western-central Europe (von Raumer et al. 2014), is documented by widespread occurrences of durbachites which typically form NNE–SSW oriented belts in the Bohemian Massif (Janoušek et al. 2020). For instance, the largest durbachite intrusion occurring in the Bohemian Massif, the Třebíč pluton (U–Pb zircon ~ 335 Ma; Schaltegger et al. 2021), was originally around twice larger than today and its marginal part reached the tectonic boundary between the Moldanubian Zone and the Svratka Complex where the studied U-deposits are situated (Leichmann et al. 2017). The tectonic boundary between the high-grade Gföhl Unit and the medium-grade Svratka Complex, mainly composed of metapelites, corresponds to a low angle thrust between these two Moldanubian subunits (Tajčmanová et al. 2006).

The Western Moravian U-province

The studied U-deposits in the eastern part of the Moldanubian Zone are typically bound to NNW-SSE-striking ductile shear zones developed in the high-grade metasedimentary basement (Fig. 1b). The origin of the shear zones is compatible with SW–NE normal and N–S dextral kinematics (Kříbek and Hájek 2005). These faults can be 10–15 km long, occasionally up to 25–30 m wide, and persist to depth in excess of 1 km (Dahlkamp 2016). Longitudinal fault structures hosting U-mineralization are crosscut and segmented by steep, ductile to brittle NW–SE- and SW–NE-striking fault zones that host post-U carbonate-quartz-sulfide mineralization.

Accordingly, Kříbek et al. (2009) distinguished three major mineralization substages of the uraniferous hydrothermal event that formed the largest Moldanubian U-deposit (the Rožná deposit with total mine production of 23 000 t U): (1) pre-U quartz-sulfide and carbonate-sulfide mineralization, (2) U-mineralization, and (3) post-U quartz-carbonate-sulfide mineralization. The pre-U mineralization substage, dated by K–Ar ages of authigenic K-feldspar (296–281 Ma; Kříbek et al. 2009) and K–Ar sericite ages (307–304 Ma; Arapov et al. 1984), was linked to the exhumation of the Moldanubian orogenic root. The pre-ore substage was characterized by temperatures of about 300 °C (Kříbek and Hájek 2005) and its fluid inclusion compositions indicate large-scale mixing of basinal brines with meteoric water (Kříbek et al. 2009). The widespread influx of oxidized basinal fluids into the crystalline basement of the Moldanubian Zone is reflected by pervasive hematitization, albitization, and dequartzification of the host metamorphic rocks. In this context, Kříbek et al. (2009) suggested that U was leached from the surrounding metamorphic rocks during this substage, with regard to the lack of any exposed granitic rocks in the vicinity of the U-deposits (Dahlkamp 2016). The main ore-substage, recorded by U–Pb bulk-uraninite and monazite ages and K–Ar illite dates in the range of ca. 280–260 Ma (Anderson et al. 1988; Kříbek et al. 2009), coincides with the transcurrent reorganization of crustal blocks of the Bohemian Massif and with Late Stephanian-Early Permian rifting. Fluid-inclusion studies coupled with chlorite thermometry suggest a temperature decrease (150–170 °C) and contribution of basinal brines during the ore-substage (Kříbek et al. 2009). The post-U substage was dated by K–Ar sericite ages (233–227 Ma; Kříbek and Hájek 2005), corresponding to the early Tethys-Central Atlantic rifting and tectonic reactivation of the Variscan structures of the Bohemian Massif. Low-temperature (< 100–178 °C) mixing of several types of fluids was estimated by fluid inclusion studies (Hein et al. 2002).

In the Western Moravian U-province, three different U-mineralization types were previously described (Arapov et al. 1984; Dahlkamp 2016; Kříbek et al. 2009). The first type includes the network-disseminated coffinite > uraninite mineralization occurring in narrow subparallel ore bodies formed along longitudinal, shear, and cataclasite zones. These cataclasite U ore zones are ordinarily enriched in graphite and typical alteration processes include chloritization, pyritization, and carbonization. The second type of U-mineralization represents vein-type ore with a characteristic predominance of uraninite over late coffinite in carbonates predominantly forming calcite veins. These uraninite-bearing veins usually occur in tension gashes and horsetail-like structures of subsidiary faults genetically related to the master faults (Dahlkamp 2016; Kříbek et al. 2009). The third type corresponds to the metasomatic

type, episyenite-like mineralization exclusively described in the Rožná deposit (Kříbek et al. 2009), involving disseminated coffinite and uraninite in dequartzified, chloritized, albitized and hematitized gneisses adjacent to shear zones (Dahlkamp 2016). This study focuses solely on the second type of U-mineralization, corresponding to the hydrothermal uraninite-carbonate veins, that likely coincides with the main U-mineralizing events in the European Variscides (Kříbek et al. 2009).

Sampling and analytical methods

We collected 9 samples of U-mineralization from the Rozsochy, Rožná-Jasan and Brzkov deposits (Fig. 1b, c) (3 samples for each locality), that come from archives of the Moravian Museum and DIAMO s.e. (organization dealing with the remediation of former U mining activities), because these U mines are no longer accessible. Building upon our previous findings (Wertich et al. 2022), these particular U-deposits were selected to explain the origin of their unusual chemical composition (significantly high HFSE and REE content) and thus provide insight into their metallogenetic model, which is also applicable to other vein-type U-deposits in the Moldanubian Zone. Polished thin sections of selected ore samples were used for detailed studies involving reflected-light microscopy and backscattered-electron (BSE) imaging in order to precisely earmark unaltered uraninite domains suitable for electron microprobe (EMP), laser ablation-inductively coupled plasma-mass spectrometry (LA-ICP-MS), and secondary-ion mass spectrometry (SIMS) analyses.

In addition, we collected 18 samples of ultrapotassic rocks (Fig. 1b) within the Třebíč pluton (Pocoucov = POC, Petrůvky = PET, Třebíč = TRE, Velké Meziřící = V-MEZ) and its smaller satellite body near Nové Město na Moravě (Slavkovice = SLA). We mainly focused our studies on major primary U-bearing phases and their alteration products in ultrapotassic rocks to provide constraints on a possible genetic link between these lithologies and U-deposits.

BSE images along with mineral chemistry were obtained by EMP Cameca SX 100 at the Department of Geological Sciences, Masaryk University, Brno. Operating conditions for spot analyses were as follows: wavelength-dispersive mode, accelerating voltage of 15 kV, beam current of 6–20 nA, and beam size of 2–6 μm for primary accessory phases and their alteration products (zircon, thorite, uraninite, titanite, allanite, monazite, REE-fluorocarbonate), 5 μm for silicates (amphibole, biotite, chlorite) and U-mineralization (uraninite), and 10 μm for apatite. The following natural and synthetic standards were used: sanidine (K, Al), titanite (Si, Ti), albite (Na), fluorapatite (P, Ca), pyrope (Mg), almandine (Fe), vanadinite (Cl, Pb), zircon (Zr), columbite (Nb), ThO_2

(Th), UO_2 (U), $ScVO_4$ (Sc, V), topaz (F). Detection limits of EMP analyses of accessory phases are provided in ESM Table A. Chlorite thermometry (Cathelineau 1988; Jowett 1991) was applied to chlorite after biotite from ultrapotassic rocks in order to estimate the temperature of chloritization of primary biotite. EMP element distribution maps were acquired with an accelerating voltage of 15 kV, step size of 1 μm using a fully focused electron beam, and dwell time of 0.1 s. In situ Th-U-total Pb EMP dating was used to obtain age estimates of magmatic uraninite in ultrapotassic rocks. As an independent reference material, two monazite samples of well-known ages (Pb-Pb TIMS-EVA 498 ± 2 Ma, U–Pb ICP-MS 336 ± 2 Ma; see Moiny et al. 2020 for details) were measured prior and after the samples under investigation.

Trace element concentrations were measured by LA-ICP-MS at the Department of Chemistry, Masaryk University, Brno, using an Analyte G2 laser ablation device and Agilent 7900 ICP-MS analyser with an octopole reaction cell. The laser operates at a wavelength of 193 nm with a pulse duration ≤ 4 ns. Helium as a carrier gas with a flow rate of 0.65 L min⁻¹ was used. The aerosol was mixed with argon serving as makeup gas with flow rate 1 L min⁻¹ and transported to the ICP-MS. The mass spectrometer operated at the forwarded power of 1550 W and Ar gas flow rate of 15 L min⁻¹ (outer plasma gas). Ablation spot was from 30 to 50 μm in diameter, regarding the area analyzed. Repetition rate was 10 Hz and fluence 4 J cm⁻². One spot was analyzed for 60 s. Total integration time was 4.1 s. External calibration was performed using the standard reference materials (SRM) NIST 610 and NIST 612. The LA-ICP-MS output was evaluated using the software Ilaps (Faltusová et al. 2022), especially developed for LA-ICP-MS data reduction.

The whole-rock major element composition was determined by Acme Labs Vancouver (Bureau Veritas) by ICP-OES after fusion with lithium borate flux. Trace elements, including REE, were analyzed using ICP-MS with additional lithium tetraborate fusion. Moreover, incompatible transition metals (Ni, V, Sc) were determined by ICP-MS after modified aqua regia digestion. For more analytical details, reproducibility, and detection limits see https://commodities.bureauveritas.com.

U–Pb apatite dating in combination with apatite fission-track (AFT) thermochronology were performed at GeoSep Services (GSS) laboratory, Idaho. Apatite grains were separated from the original sample material using standard procedures combined with specific customized procedures described by Donelick et al. (2005). Spontaneous tracks were first counted on all apatite mounts in unpolarized light at 2000 × magnification. Kinetic information (D_{par}) was collected from every apatite grain analyzed. An Agilent 7700 × quadrapole ICP-MS equipped with a New Wave Nd-YAG 213 nm laser ablation system was then used to measure isotopic data necessary for AFT and U–Pb

age calculations from the same regions on the individual grains from which the spontaneous tracks were initially counted. For all laser analyses, the beam diameter was 20 μm and the frequency was set at 5 Hz, yielding ablation pits 16–18 μm deep. Fission-track ages were calculated using: (a) the ratio of the density of natural fission tracks present in the grain to the amount of ^{238}U present, and (b) a modified version of the radioactive decay equation that includes an LA-ICP-MS zeta calibration factor (Donelick et al. 2005). U–Pb ages were analyzed and calculated following an iterative Stacey and Kramers (1975) terrestrial Pb evolution model after Chew et al. (2012) and Thomson et al. (2012).

The U–Pb ages for U-mineralization were determined from measurements of the isotopes of U, Pb, and Th using SIMS (ESM Table B). The isotopic compositions of uraninite samples were acquired with the ion microprobe CAMECA IMS 1280-HR at CRPG-CNRS (Nancy, France). The primary O$^-$ ion beam was accelerated at 13 kV, with a primary current intensity ranging between 3.5 and 5 nA. The size of each analysis spot was ∼ 15 μm. Positive secondary ions were extracted with a 10 kV potential, and the spectrometer slits were set for a mass resolving power of ∼ 6000 to separate isobaric interferences of REE dioxides from Pb. The relative sensitivity factor between Pb and U used for samples was determined from an empirical linear relationship defined between UO^+/U^+ and Pb^+/U^+ (Deloule et al. 2002) from all the measurements performed on the reference uraninite (Zambia, concordant age of 540 ± 4 Ma; Cathelineau et al. 1990). The correction for a common lead contribution was made by measuring the amount of ^{204}Pb and then calculating the common lead composition utilizing the model of Stacey and Kramers (1975). Uncertainties in ages are reported at the 2σ level.

Airborne gamma-ray spectrometry information is from surveys in the 1980s. An AN-2 fixed-wing airplane equipped with a four-channel gamma-ray spectrometer Exploranium DiGRS 3001 was used. The flight line distance was 250 m with an airspeed of 130–140 km h^{-1} and ground clearance of 80–100 m. A sampling interval of one second was used, so the data were collected each 40 m along the flight lines.

Results

Within this section, we successively provide the petrographic, geochemical and geochronological characteristics of the U-deposits (hydrothermal vein-type mineralization) from the Western Moravian U-province and the ultrapotassic plutons (durbachite series) occurring in the Gföhl Unit of the Moldanubian Zone.
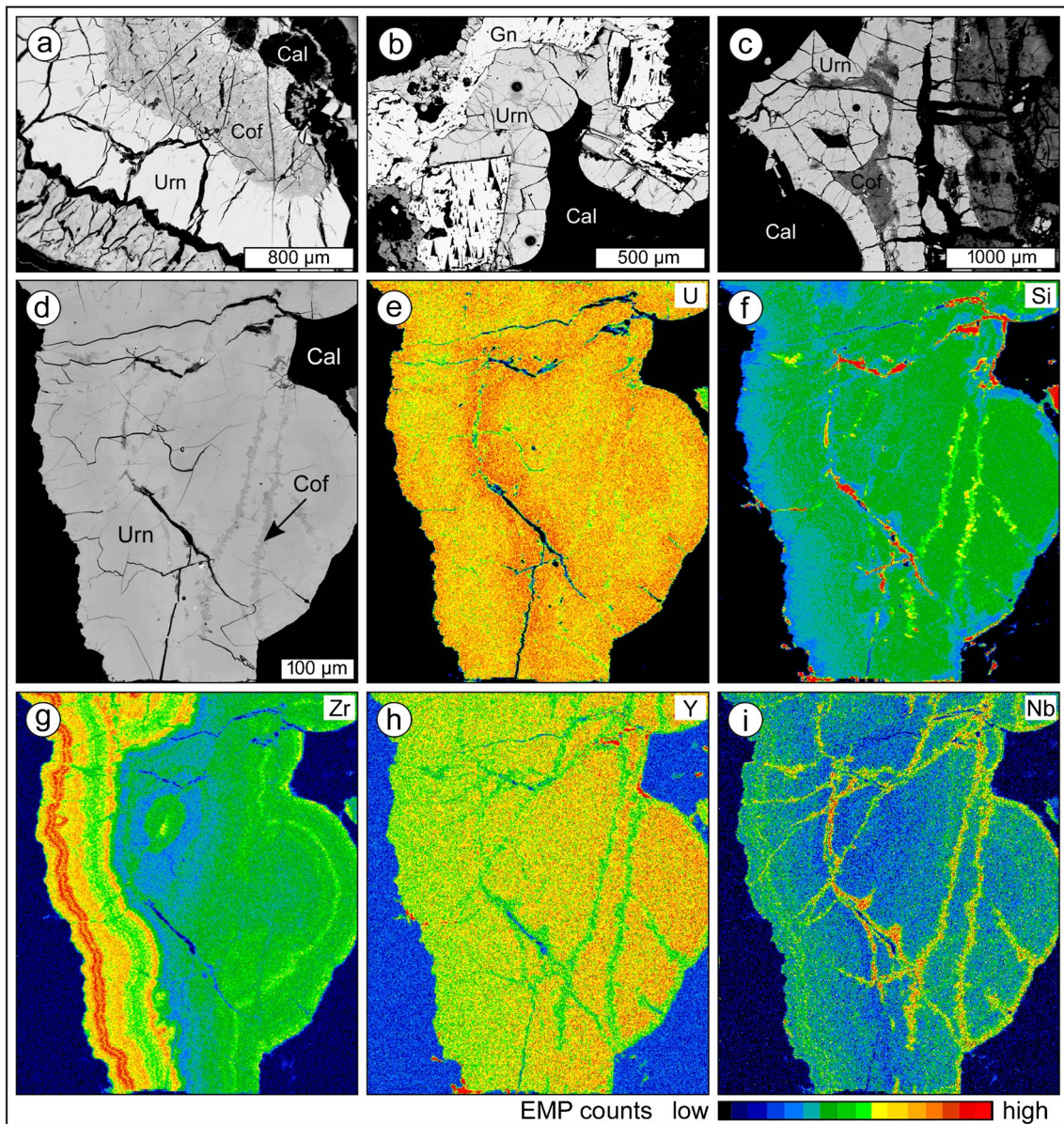
U-mineralization

Mineral assemblages, textures, and chemistry of the U-mineralization

The studied uraninite samples from the Rozsochy, Rožná-Jasan, and Brzkov deposits are characterized by similar textural features (Fig. 2a–i) typical of low-temperature hydrothermal vein-type U-mineralization (Křížek et al. 2009) within the entire Variscan Orogenic Belt (e.g., Ballouard et al. 2018; Marignac and Cuney 1999; Velichkin and Vlasov 2011). Uraninite ordinarily forms massive aggregates with colloform/botryoidal textures that are usually surrounded or crosscut by veinlets of hydrothermal calcite (Fig. 2a–d). The U-mineralization is typically hosted in thick hydrothermal carbonate veins predominantly composed of calcite. Uraninite aggregates are occasionally brecciated within some samples and locally associated with coffinite and sulfides (pyrite, chalcopyrite, galena) (Fig. 2b) from the pre-U ore stage (Křížek et al. 2009). Almost all uraninite samples are affected by a variable degree of coffinitization (Fig. 2a–i); thus, we selected for further analytical techniques (EMP, LA-ICP-MS, SIMS) only unaltered aggregates and/or domains of uraninite showing no visible effects of coffinitization, tested with BSE imaging and EMP analyses.

The uraninite samples from individual deposits are characterized by relatively variable chemical composition (Table 1). Uraninite from the Rožná-Jasan deposit shows slightly higher UO_2 contents (87.26–89.43 wt%) compared to Rozsochy and Brzkov deposits (82.75–86.46 wt%). Despite variable CaO content (2.19–8.25 wt%) among different deposits, within each sample CaO content is relatively uniform (Fig. 3a), indicating that calcium was incorporated during uraninite crystallization with only limited contribution of post-crystallization alteration. Accordingly, it should be noted that EMP analyses of unaltered uraninite aggregates and/or domains showing no visible effects of alteration (mainly coffinitization; see Fig. 3b) are presented in the current study (Table 1), as demonstrated by their low SiO_2 concentrations (≤ 3.48 wt%). Content of PbO in uraninite from individual deposits commonly varies from 2.65 to 3.70 wt% and negatively correlates with SiO_2 concentrations (Fig. 3b), likely reflecting partial lead loss caused by post-crystallization incipient alteration.

Trace element concentrations in uraninite

The characteristic feature of uraninite from the studied deposits is their anomalous HFSE enrichment (especially Zr, Nb, Ti) (Table 2) similar to that of granite/pegmatite-hosted U-deposits (Fig. 3c, d). Uraninite from the Rozsochy deposit shows the highest contents of Zr (up to 1.61 wt%), Nb (up to 0.67 wt%) and Ti (up to 0.45 wt%). Such extreme

Fig. 2 BSE images (**a–d**) and EMP elemental distribution maps (**e–i**) of studied samples of vein-type U-mineralization from the **a** Rožná-Jasan, **b** Brzkov, **c–i** Rozsochy deposits (see Fig. 1b) illustrating characteristic massive and colloform textures of analyzed uraninite, its close association with common gangue minerals and variable intensity of coffinitization. Note that only unaltered uraninite domains were analyzed in the current study. Abbreviations: Urn = uraninite, Cof = coffinite, Cal = calcite, Gn = galena

HFSE enrichment was also confirmed by EMP analyses (Zr ≤ 2.32 wt%, Nb ≤ 0.53 wt%, Ti ≤ 0.48 wt%) (Table 1). As revealed by EMP imaging, HFSE (except for Nb) are incorporated within the structure of hydrothermal uraninite, precluding the presence of HFSE-rich micro-inclusions or effects of late alteration which can affect initial trace element distribution in uraninite (Martz et al. 2019a), as evidenced in case of Nb enrichment typical for slightly coffinitized domains (Fig. 2i). Uraninite from the Rožná-Jasan deposit has comparable trace element signatures with somewhat lower Zr (≤ 0.47 wt%) and Ti (≤ 0.16 wt%) contents and notably low Nb (~ 10 ppm) content relative to the Rozsochy deposit. Uraninite from the Brzkov deposit exhibits high Ti (≤ 0.39 wt%) contents and rather low Zr (≤ 680 ppm) and Nb (≤ 36 ppm) concentrations. Additionally, uraninite from the Brzkov deposit shows notably high total REE contents (∑REE up to 1.12 wt%) in contrast to Rozsochy (≤ 3400 ppm) and Rožná-Jasan (≤ 790 ppm) deposits. High Y (up to 0.40 wt%) contents in uraninite from the Rozsochy and Brzkov deposits are also noticeable.

Chondrite-normalized (McDonough and Sun 1995) REE patterns of uraninite considerably differ between individual

Table 1 EMP analyses of vein-type U-mineralization from the Moldanubian deposits

Deposit	ROZ	ROZ	ROZ	ROZ	DRJ	DRJ	DRJ	DRJ	BRZ	BRZ	BRZ	BRZ	D.L
Major oxides (wt%)													
UO_2	83.12	83.59	83.54	83.77	87.74	87.43	87.89	87.75	83.96	83.34	82.79	83.65	0.06
SiO_2	2.36	3.28	3.37	2.42	3.22	3.26	2.99	3.23	1.57	1.68	0.95	1.69	0.02
TiO_2	0.08	0.11	b.d.l	0.47	0.09	0.06	0.14	0.18	b.d.l	b.d.l	b.d.l	b.d.l	0.04
ZrO_2	1.12	3.14	2.85	0.07	0.60	0.62	0.42	0.47	b.d.l	b.d.l	b.d.l	b.d.l	0.04
CaO	4.11	2.19	2.25	4.30	3.87	4.21	4.07	4.00	7.23	7.30	8.25	7.33	0.02
PbO	2.92	2.76	2.83	2.89	2.82	2.79	2.86	2.87	3.36	3.27	3.70	3.36	0.02
FeO	0.51	0.82	0.86	0.58	0.86	0.94	0.94	0.84	0.09	0.21	0.09	0.10	0.04
Y_2O_3	0.19	b.d.l	b.d.l	0.20	b.d.l	b.d.l	b.d.l	b.d.l	b.d.l	b.d.l	b.d.l	b.d.l	0.03
V_2O_3	0.53	0.51	0.51	0.69	0.34	0.35	0.34	0.37	0.54	0.49	0.66	0.61	0.03
Nb_2O_5	0.33	0.20	0.21	0.28	0.13	0.16	0.18	0.16	b.d.l	b.d.l	b.d.l	b.d.l	0.04
P_2O_5	0.20	0.15	0.16	0.24	b.d.l	b.d.l	b.d.l	b.d.l	0.18	0.16	0.18	0.17	0.02
F	0.37	b.d.l	b.d.l	0.47	b.d.l	b.d.l	b.d.l	b.d.l	0.34	0.38	0.33	0.17	0.06
Total	95.8	96.7	96.6	96.4	99.7	99.8	99.8	99.9	97.3	96.8	96.9	97.1	
Mineral formulae (apfu)													
U	0.738	0.717	0.718	0.737	0.743	0.735	0.746	0.740	0.743	0.738	0.739	0.736	
Si	0.094	0.127	0.130	0.096	0.123	0.123	0.114	0.122	0.063	0.067	0.038	0.067	
Ti	0.003	0.003	0	0.014	0.003	0.002	0.004	0.005	0	0	0	0	
Zr	0.022	0.059	0.054	0.001	0.011	0.011	0.008	0.009	0	0	0	0	
Ca	0.176	0.091	0.093	0.182	0.158	0.170	0.166	0.162	0.308	0.311	0.355	0.311	
Pb	0.031	0.029	0.029	0.031	0.029	0.028	0.029	0.029	0.036	0.035	0.040	0.036	
Fe	0.017	0.027	0.028	0.019	0.027	0.030	0.030	0.027	0.003	0.007	0.003	0.003	
Y	0.004	0	0	0.004	0	0	0	0	0	0	0	0	
V	0.017	0.016	0.016	0.022	0.010	0.011	0.010	0.011	0.017	0.016	0.021	0.019	
Nb	0.006	0.003	0.004	0.005	0	0	0	0	0	0	0	0	
P	0.007	0.005	0.005	0.008	0.004	0.005	0.006	0.005	0.006	0.005	0.006	0.006	
F	0.047	0	0	0.059	0	0	0	0	0.043	0.048	0.042	0.021	

Cation proportions calculated based on a total of two oxygen atoms per formula unit

ROZ = Rozsochy; DRJ = Rožná-Jasan; BRZ = Brzkov; D.L. = detection limits; b.d.l. = below detection limits
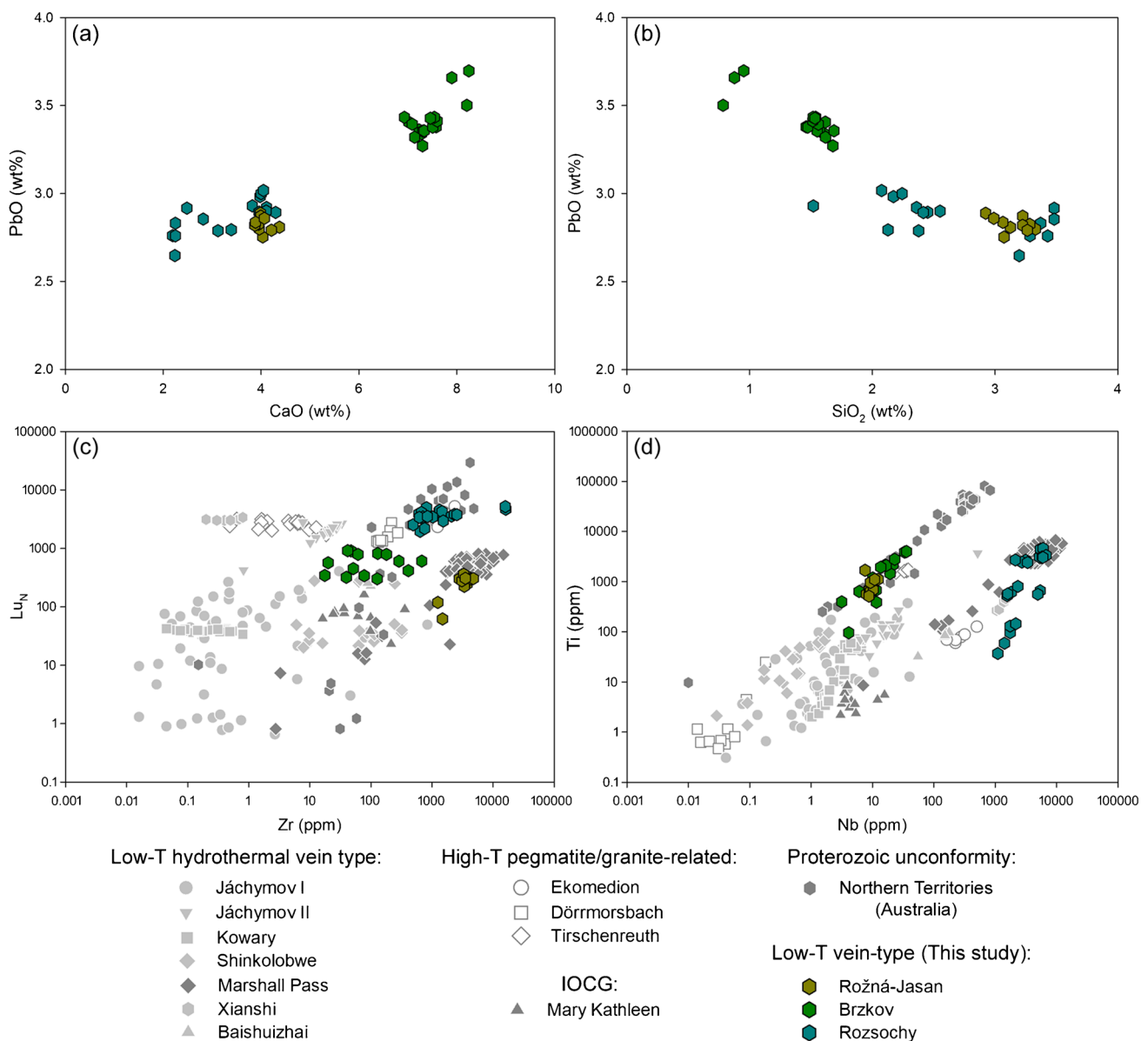
Fig. 3 **a** CaO vs. PbO, **b** SiO_2 vs. PbO, **c** Zr vs. Lu_N, and **d** Nb vs. Ti plots showing the chemical composition of analyzed uraninite samples. Abundances of minor elements (Ca, Pb, Si) were determined by EMP, whereas trace element concentrations (Zr, Lu, Nb, Ti) were measured by LA-ICP-MS. Trace element signatures of uraninite from various deposit types are from Balboni et al. (2016), Bonnetti et al. (2018), Corcoran et al. (2019), Frimmel et al. (2014). Content of Lu is normalized to chondritic values from McDonough and Sun (1995)

deposits (Fig. 4a–c). Uraninite from the Rozsochy deposit features HREE-enriched patterns ($La_N/Yb_N \sim 0.02$–0.09) with well-pronounced negative Eu ($Eu_N/Eu_N^* \sim 0.04$–0.06; $Eu_N^* = \sqrt{(Gd_N \times Sm_N)}$) and positive Ce anomaly ($Ce_N/Ce_N^* \sim 1.40$–2.74; $Ce_N^* = \sqrt{(La_N \times Pr_N)}$). Uraninite from the Rožná-Jasan deposit has rather flat REE patterns ($La_N/Yb_N \sim 0.61$–0.91) with less pronounced negative Eu anomaly ($Eu_N/Eu_N^* \sim 0.44$–0.57) compared to the Rozsochy deposit. Uraninite from the Brzkov deposit is characterized by LREE-enriched patterns ($La_N/Yb_N \sim 3.32$–9.29) with weak Eu anomaly ($Eu_N/Eu_N^* \sim 0.74$–0.84).

In situ *U–Pb isotopic dating*

Based on BSE imaging and EMP analyses of uraninite from the Rozsochy deposit, the largest and most suitable areas of U-mineralization were selected for U–Pb in situ dating by SIMS (ESM Table B). Special caution was taken in selecting uraninite domains devoid of post-crystallization alteration and sulfide inclusions, having relatively uniform U and Pb contents along with low Si contents. Overall, the 36 analyses plot in concordant to discordant positions in the Wetherill diagram indicating more or less significant radiogenic

Table 2 LA-ICP-MS analyses (ppm) of vein-type U-mineralization from the Moldanubian deposits

Deposit	ROZ	ROZ	ROZ	ROZ	ROZ	DRJ	DRJ	DRJ	DRJ	DRJ	BRZ	BRZ	BRZ	BRZ	BRZ	D.L
Sc	184	79	210	194	82	45	30	40	43	43	69	63	67	59	59	2
Ti	3012	3121	2681	659	2410	705	1686	1107	1116	965	677	2179	1452	3873	2797	6
V	2972	3768	3952	3351	3216	2509	3519	2249	2880	2389	1534	1569	1686	1669	1465	2
As	3607	3340	3996	3553	3879	4482	4387	4322	5144	4265	2383	3714	2946	3098	2772	60
Sr	484	954	798	682	1210	895	672	400	521	859	358	402	420	360	370	0.4
Y	3021	2238	3673	3111	2863	563	197	531	539	524	1991	1914	1779	1948	1952	0.2
Zr	16,137	2331	15,851	15,978	1524	3086	1246	3514	4068	4731	42	129	61	679	179	0.2
Nb	5670	5826	4947	5395	2156	8.8	7.6	10.9	12	9.2	11	22	19	34	23	0.2
Sb	863	559	720	644	582	1534	1467	1508	1959	1417	3833	9812	5643	10,567	6316	2
La	68	26	36	26	15	60	27	58	67	69	870	937	891	807	854	0.08
Ce	336	213	134	112	68	130	71	141	150	133	3293	3580	3030	2569	3081	0.08
Pr	35	16	15	12	6	23	13	26	26	22	625	645	627	430	552	0.04
Nd	171	72	87	67	35	120	62	133	142	113	3211	3200	3123	2271	2735	0.1
Sm	134	72	77	65	35	41	21	47	49	40	851	899	884	624	755	0.4
Eu	2.2	1.3	1.4	1.3	0.9	9.0	3.3	10	10	8	200	202	199	155	174	0.04
Gd	203	142	174	142	92	63	25	66	66	58	657	682	618	524	591	0.6
Tb	65	54	54	47	29	11	5	12	13	11	100	88	89	65	79	0.08
Dy	557	479	489	444	260	84	35	94	98	84	532	484	482	371	435	0.2
Ho	116	100	111	102	61	18	7	20	21	18	83	76	75	62	71	0.06
Er	474	411	465	454	257	57	23	63	66	57	228	203	189	161	188	0.08
Tm	83	68	84	76	45	8	4	9	10	9	32	28	27	22	27	0.04
Yb	699	597	770	669	390	56	25	63	64	59	171	150	151	115	140	0.2
Lu	115	94	128	116	72	7.1	2.9	7.6	7.8	7.5	22	20	19	15	19	0.04
$\sum$REE	3060	2346	2626	2334	1368	687	324	750	790	689	10,875	11,194	10,405	8190	9702	
La_N/Yb_N	0.07	0.03	0.03	0.03	0.03	0.73	0.75	0.62	0.71	0.79	3.46	4.24	4.00	4.76	4.15	
Eu_N/Eu_N^*	0.04	0.04	0.04	0.04	0.05	0.53	0.44	0.57	0.55	0.52	0.81	0.79	0.82	0.83	0.79	

ROZ = Rozsochy; DRJ = Rožná-Jasan; BRZ = Brzkov; D.L. = detection limits
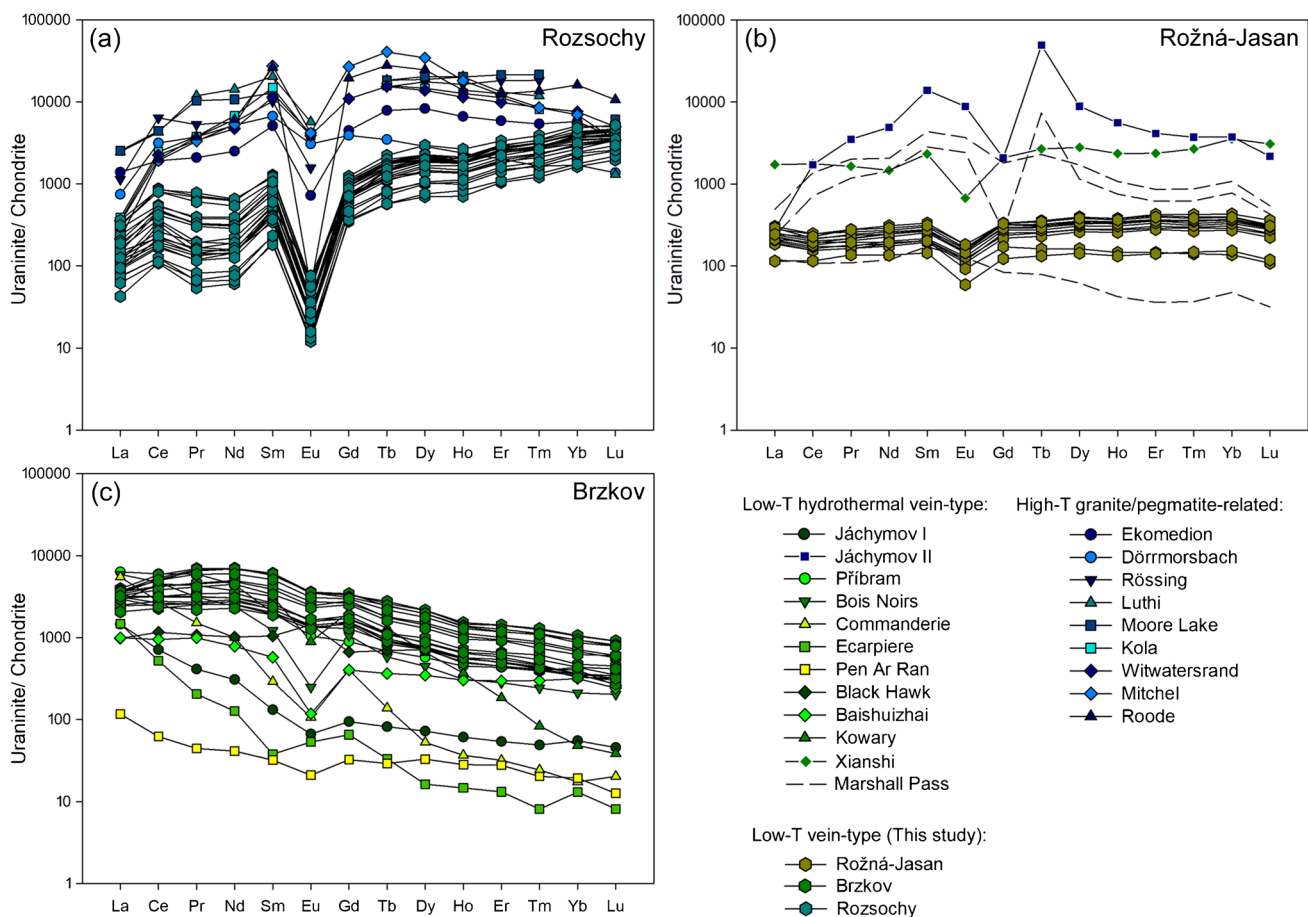
Fig. 4 **a–c** Chondrite-normalized REE patterns of uraninite from the studied deposits, standardized values are from McDonough and Sun (1995). REE composition (in median values) of uraninite from low-T hydrothermal vein-type and high-T granite/pegmatite-related deposits is from Alexandre et al. (2015), Balboni et al. (2016), Ballouard et al. (2017), Bonnetti et al. (2018), Corcoran et al. (2019), Depiné et al. (2013), Frimmel et al. (2014), Mercadier et al. (2011a)
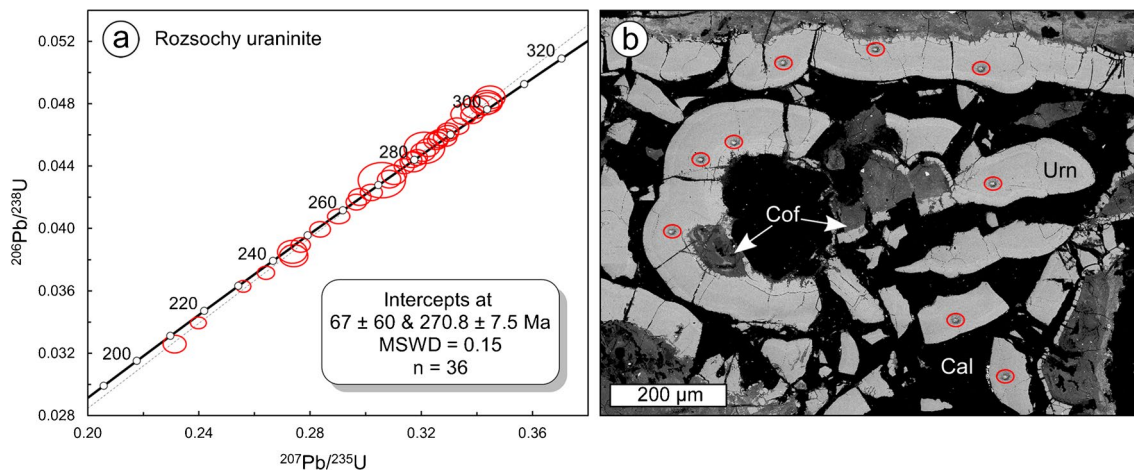
Fig. 5 **a** Wetherill concordia diagram displaying SIMS analyses performed on uraninite from the Rozsochy deposit. **b** BSE image of the uraninite sample analyzed in this study. The red ellipses indicate the location of SIMS data points. Abbreviations: Urn = uraninite, Cof = coffinite, Cal = calcite
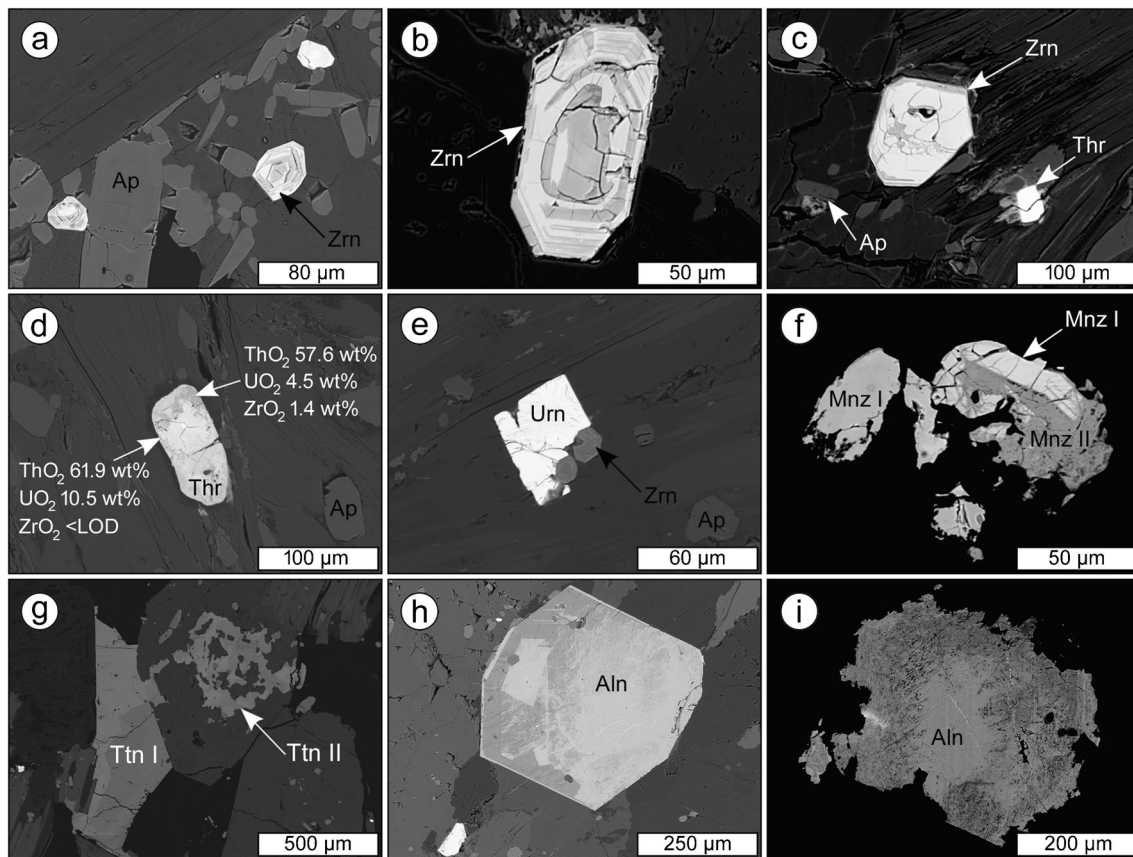
Fig. 6 BSE images of the main primary accessory phases in ultrapotassic rocks. **a** Pristine prismatic apatite and slightly altered zircon enclosed in mafic silicates. **b** Hydrothermal alteration of metamict zircon typically manifested by low BSE intensity. **c** Dissolution of zircon and U-rich thorite triggering extensive HFSE remobilization (BSE-brighter areas) along cleavage plains and grain boundaries of surrounding rocks-forming minerals. **d** Partially altered U-rich thorite showing different chemistry between BSE brighter (less altered) and darker domains (extensively altered). **e** Preserved primary mag-matic uraninite. **f** Fluid-driven decomposition of primary Th-rich monazite (Mnz I) to monazite (Mnz II) chemically corresponding to rhabdophane. **g** Early magmatic euhedral titanite (Ttn I) along with late-magmatic irregular titanite (Ttn II). **h** Slightly altered primary allanite showing patchy zonation. **i** Extensively altered allanite with high porosity. Abbreviations: Zrn = zircon, Ap = apatite, Thr = thorite, Urn = uraninite, Mnz = monazite, Ttn = titanite, Aln = allanite, LOD = limit of detection

Pb loss caused by a post-crystallization alteration (Fig. 5a, b). The data define a well-constrained upper intercept of 270.8 ± 7.5 Ma (MSWD = 0.15), corresponding to crystallization age of uraninite in the Rozsochy deposit.

Ultrapotassic plutons

Petrology, mineral textures, and chemistry

The petrographic features of ultrapotassic plutons of the durbachite series have been previously described by many authors (e.g., Janoušek et al. 2020; Kotková et al. 2010); thus, only a brief petrographic description of studied samples is given here.

Despite some petrographic variability (e.g., biotite/amphibole ratio, presence or not of magmatic foliation),
the durbachite plutons are composed of coarse-grained porphyritic rocks with K-feldspar phenocrysts set in a matrix consisting of biotite, amphibole, K-feldspar, plagioclase, and a variable amount of quartz. The sub- to euhedral perthitic K-feldspar phenocrysts (up to 2.3 cm) show concentric zoning. Pleochroic biotite in matrix forms subhedral flakes (0.2–4.5 mm). Pale green, weakly pleochroic amphibole occurs as sub- to euhedral grains (0.4–5.8 mm) in association with biotite. Sub- to anhedral plagioclase is common constituent of the matrix together with anhedral perthitic K-feldspar. The most abundant accessory phase is apatite (up to 2.5 vol%). Other primary accessory minerals are zircon, U-rich thorite, uraninite, Th-rich monazite, titanite and allanite (Fig. 6a–i). Hydrothermal accessory minerals include Zr-Th-U-Si phase associated with altered zircon, REE-fluorocarbonate, F-rich titanite, Th-poor monazite (Fig. 7a–f). A summary of characteristic features
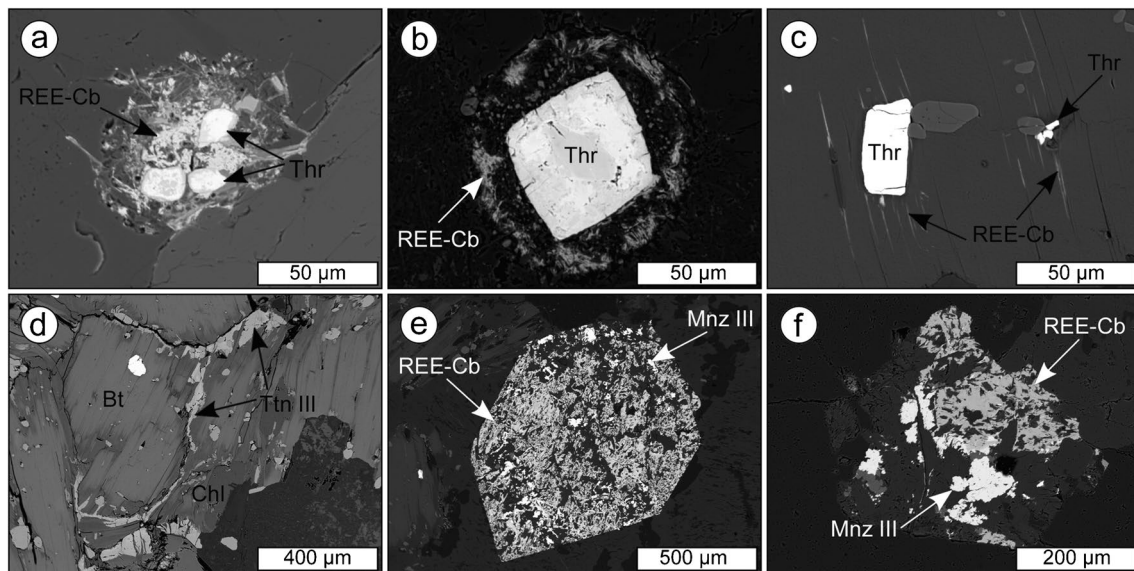
Fig. 7 BSE images of characteristic hydrothermally-derived phases in ultrapotassic rocks. **a** Almost complete dissolution of U-rich thorite. **b** Alteration haloes composed of REE-fluorocarbonate surrounding altered U-rich thorite. **c** REE-fluorocarbonate occurring in cleavage plains of chloritized biotite enclosing altered U-rich thorite. **d** Hydrothermal F-rich titanite (Ttn III) replacing chloritized biotite. **e** Pseu-domorphs of REE-fluorocarbonate and hydrothermal monazite (Mnz III) after magmatic allanite. **f** Irregular aggregates of REE-fluorocarbonate closely associated with Mnz III. Abbreviations: Zrn = zircon, Thr = thorite, REE-Cb = REE carbonate, Ttn = titanite, Bt = biotite, Chl = chlorite, Mnz = monazite

of primary accessory minerals and their hydrothermally-derived alteration products from ultrapotassic plutons is given in Table 3.

Mafic silicates

Mafic minerals include biotite and amphibole, gradually replaced by secondary chlorite. Sub- to euhedral amphibole has uniform composition corresponding to actinolite (Mg/(Mg + Fe) = 0.72–0.75; Al 1.15–1.27 apfu). It is commonly intergrown with chloritized biotite or replaced by chlorite along its cleavage planes. These chloritized domains are depleted in major and minor components (e.g., SiO_2, TiO_2, Al_2O_3, CaO) and show low analytical totals (≥ 93 wt%) along with very low F contents (ESM Table C). Tabular biotite prevails over amphibole in most durbachite samples. Chemically, it corresponds to phlogopite (Mg/(Mg + Fe) = 0.61–0.68). Phlogopite is usually replaced by clinochlore (Mg/(Mg + Fe) = 0.60–0.79). The extensive chloritization is reflected by low K_2O (≤ 5.91 wt%) and F (≤ 0.19 wt%) content in altered phlogopite. Chlorite thermometers applied on chlorite after biotite (Cathelineau 1988; Jowett 1991) yielded similar temperatures ranging from 269 to 301 °C with an average of ~280 °C (ESM Table C).

Zircon

Zircon forms clear, pale brown to cloudy euhedral prismatic crystals (100–350 μm) enclosed in mafic silicates, K-feldspar, and allanite. Most crystals show well-developed oscillatory zoning typically underlined by lower BSE intensity due to hydrothermal alteration (Fig. 6a, b). Zircon often contains early magmatic U-rich thorite inclusions (≤ 30 μm) within its crystal cores.

The chemistry of pristine zircon grains/domains is typically uniform among studied localities (ZrO_2 ~ 64–66 wt%, SiO_2 ~ 31–34 wt%; Fig. 8a–d; Table 4). The vast majority of zircon experienced self-induced structural radiation damage (metamictization) followed by fluid-driven hydrothermal alteration, as evidenced by low BSE intensity of altered zircon grains/domains (Fig. 6a–c), enhanced concentrations of non-formula elements (e.g., Ca, Fe, Al, P; Fig. 8a), decreased ZrO_2 (45.78–63.67 wt%) and SiO_2 (22.20–30.98 wt%) contents along with deficient EMP analytical totals (86.8–98.8 wt%) (Fig. 8d; Table 4). Notably, altered zircon in the PET is significantly enriched in P_2O_5 (3.41–4.53 wt%) (Fig. 8a) relative to zircon from other localities where P_2O_5 content is routinely below detection limit (Table 1 and 4). Within all samples, altered zircon domains are usually

Table 3 Characteristics of target accessory minerals from ultrapotassic plutons

Mineral	Locality	Alteration products	Mineral textures	Zoning patterns	Key elemental concentration
Zrn	POC, PET, TRE, V-MEZ, SLA	Zr-Th-U-Si phase	Euhedral prismatic	Oscillatory	Pristine: ZrO_2 64–66 wt%; $UO_2 < 0.7$ wt% $\sum$LREE 56–7400 ppm; $\sum$HREE 330–1030 ppm Altered: $ZrO_2 < 64$ wt%; UO_2 0.3–2.8 wt% $\sum$LREE 14 ppm; $\sum$HREE 1154 ppm
Ap	POC, PET, TRE, V-MEZ, SLA	None	Sub-euhedral prismatic, anhedral rounded	None or rarely weak sectoral	$\sum$REE 5000–9900 ppm Y 400–870 ppm; U 40–130 ppm HFSE (Zr, Nb, Ta) < 10 ppm
Thr	POC, TRE, V-MEZ, SLA	REE-Cb	Anhedral-subhedral	None	Pristine: UO_2 19–30 wt%; $ThO_2 < 56.4$ wt% $ZrO_2 < 1.56$ wt%; $P_2O_5 < 0.28$ wt% Altered: $UO_2 < 16$ wt%; ThO_2 38–68 wt% $ZrO_2 < 15.77$ wt%; P_2O_5 0.20–10.37 wt%
Urn	TRE	None	Euhedral cubic	None	UO_2 82–85 wt%; ThO_2 8–11 wt%
Mnz I	PET	Mnz II	Subhedral	None or rarely weak sectoral	REE_2O_3 47–62 wt%; ThO_2 10–25 wt% UO_2 0.32–0.83 wt%
Mnz II[a]	PET		Irregular	None	REE_2O_3 34–42 wt%; ThO_2 14–24 wt% UO_2 0.15–0.38 wt%; F 0.3–0.4 wt%
Mnz III[a]	POC, PET, TRE, V-MEZ, SLA		Irregular	None	REE_2O_3 65–69 wt% ThO_2 0.6–2.1 wt%; $UO_2 < 0.08$ wt%
Ttn I	POC, V-MEZ, SLA	None	Subhedral-euhedral	Sectoral	Al_2O_3 1.0–1.8 wt% $\sum$REE < 29,600 ppm; Nb < 14,300 ppm
Ttn II	POC	None	Irregular	Patchy	Al_2O_3 1.1–1.7 wt%; SnO_2 1.0–2.6 wt%
Ttn III[a]	POC, PET, V-MEZ, SLA		Irregular	None	Al_2O_3 1.1–8.7 wt%; F up to 2.8 wt%
REE-Cb[a]	POC, PET, TRE, V-MEZ, SLA		Irregular	Irregular	REE_2O_3 43–69 wt% CaO 2–19 wt%; F 4–7 wt%
Aln	POC, SLA	REE-Cb, Mnz III	Euhedral	Sectoral (less altered), patchy (strongly altered)	Sectoral: $REE_2O_3 < 22.4$ wt% Patchy: REE_2O_3 17–20 wt% UO_2 0.11–0.38 wt%; ThO_2 0.68–2.98 wt%

Mineral abbreviations: Zrn = zircon, Ap = apatite, Thr = thorite, Urn = uraninite, Mnz = monazite, Ttn = titanite, REE-Cb = REE-fluorocarbonate, Aln = allanite, TRE = Třebíč; PET = Petrůvky; POC = Pocoucov; V-MEZ = Velké Meziříčí; SLA = Slavkovice

[a]Secondary, hydrothermally-derived phases

enriched in UO_2 and ThO_2 compared to pristine domains (Fig. 8b).

The pervasive alteration of zircon is also recorded by EMP maps showing partial to almost complete zircon dissolution in most durbachite samples (Fig. 9). Altered zircon is intimately surrounded by abundant microfractures that are usually filled by Zr-Th-U-Si phase, reflecting HFSE leaching from altered zircon (Fig. 9). EMP analyses of Zr-Th-U-Si phase document extreme enrichment in ZrO_2 (32.83–42.70 wt%), ThO_2 (2.98–4.79 wt%), and UO_2 (1.17–3.46 wt%). High F content (up to 0.53 wt%) in the Zr-Th-U-Si phase is also noticeable.
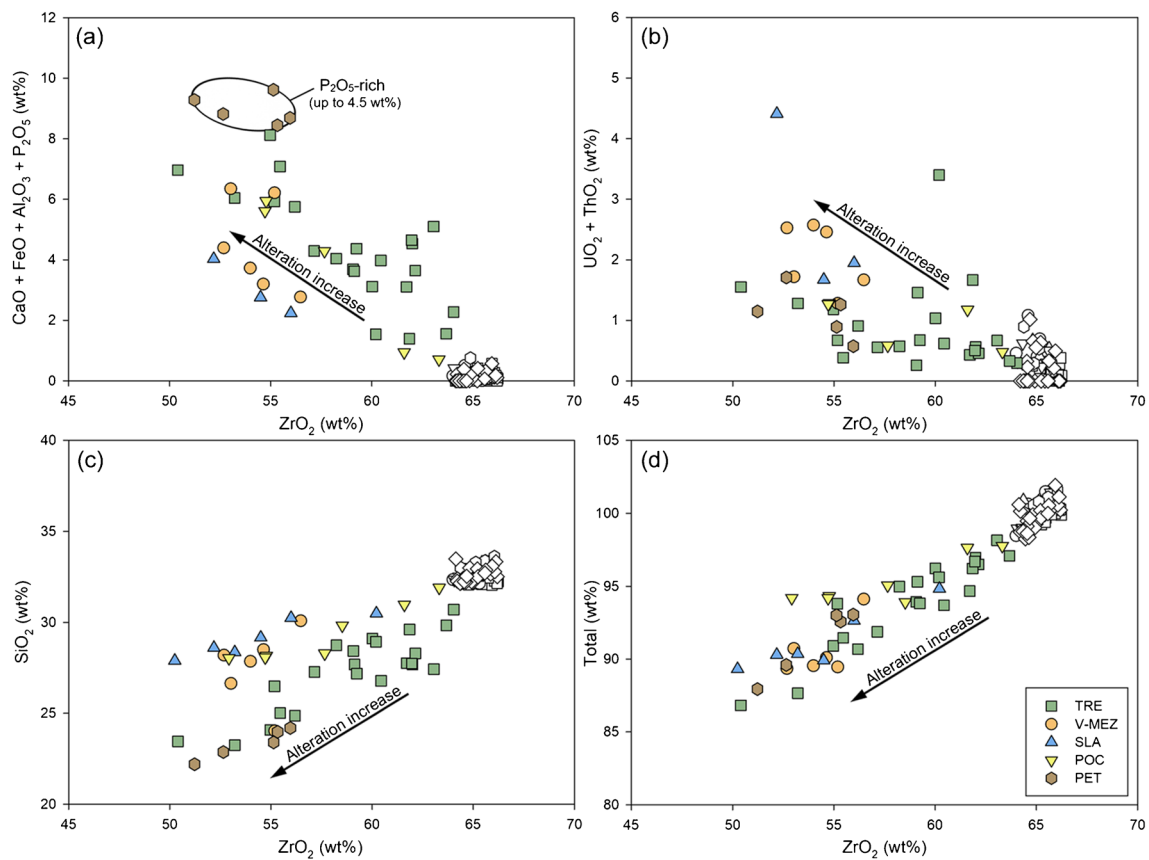
Fig. 8 Chemical composition of zircon from ultrapotassic rocks. **a** Binary plot ZrO_2 vs. $CaO+FeO+Al_2O_3+P_2O_5$, **b** ZrO_2 vs. UO_2+ThO_2, **c** ZrO_2 vs. SiO_2, **d** ZrO_2 vs. EMP total. Colored symbols correspond to altered zircon domains, whereas white symbols represent pristine unaltered zircon domains. Abbreviations of sampling localities same as in Fig. 1

Apatite

Apatite usually forms sub- to euhedral short-prismatic crystals with variable sizes (30–450 μm) and/or anhedral rounded grains of similar sizes. It is predominantly associated with mafic silicates such as amphibole and biotite. Most grains have no visible primary igneous zoning, occasionally apatite displays only weak sectoral zonation. In contrast to zircon, apatite shows no visible effect of late hydrothermal alteration (Fig. 6a).

Chemically, it corresponds to fluorapatite (F 2.79–3.58 wt%). The major and minor element composition of apatite is relatively homogeneous within and between individual localities (Table 4), with REE_2O_3 content reaching up to 0.87 wt%.

U-rich thorite

Thorite occurs as anhedral to subhedral grains (30–180 μm) commonly associated with REE-fluorocarbonates in the matrix (Fig. 7a–c) or irregular relatively small inclusions (< 20 μm) enclosed in metamict zircon. Thorite is an abundant phase in most samples, except for the PET, where Th-rich monazite usually prevails

(Table 3). Most thorite grains experienced extensive late alteration triggering partial to almost complete dissolution of primary thorite (Figs. 6c, d and 7a–c). Only a few rarely preserved pristine thorite inclusions enclosed in zircon retained their initial chemical composition characterized by relatively high ThO_2 (up to 56.4 wt%), UO_2 (up to 30 wt%), and EMP analytical totals (98.7–101.4 wt%) along with low ZrO_2 content routinely below 1 wt%. By contrast, altered thorite in the matrix shows highly variable contents of ThO_2 (38.17–68.42 wt%), UO_2 (0.44–15.71 wt%), ZrO_2 (≤ 15.77 wt%), P_2O_5 (0.20–10.37 wt%), F (0.19–2.09 wt%), and low analytical totals (79.1–95.9 wt%) (Table 4). Notably, less altered BSE-brighter thorite domains tend to have higher ThO_2 and UO_2 contents relative to more altered BSE-darker domains (Fig. 6d). These extensively altered BSE-darker thorite domains are generally enriched in ZrO_2, P_2O_5, Ce_2O_3, and F (Table 3 and 4).

Uraninite

Primary magmatic uraninite was rarely observed in samples from the TRE (Table 3). Uraninite occurs as euhedral cubic

Table 4 EMP analyses of accessory minerals and their possible alteration products from ultrapotassic rocks

Mineral	Pristine zircon				Altered zircon				Zr-Th-U-Si[a]		Pristine thorite		Altered thorite				
Sample	PET	TRE	V-MEZ	SLA	PET	TRE	V-MEZ	SLA	PET	POC	V-MEZ[b]	SLA[b]	PET[c]	POC[d]	TRE[c]	V-MEZ[d]	SLA[c]
Major oxides (wt%)																	
SiO_2	32.42	32.52	32.79	32.97	23.40	23.46	30.08	28.36	26.31	27.83	19.01	19.45	10.98	13.90	17.38	17.14	17.64
ZrO_2	65.80	66.12	65.45	65.44	55.13	50.40	56.48	53.21	36.91	34.22	1.56	b.d.l	7.33	0.27	12.77	b.d.l	b.d.l
UO_2	b.d.l	b.d.l	b.d.l	0.29	0.45	1.02	0.97	0.96	3.43	3.05	19.38	23.82	0.98	10.81	1.49	10.80	2.20
ThO_2	b.d.l	b.d.l	b.d.l	b.d.l	0.44	0.53	0.69	0.95	2.98	3.25	56.48	53.46	54.52	51.84	49.50	60.05	59.42
HfO_2	1.69	1.44	2.90	1.38	1.14	1.65	1.08	1.15	0.51	0.54	b.d.l	b.d.l	b.d.l	b.d.l	b.d.l	b.d.l	b.d.l
TiO_2	b.d.l	b.d.l			0.69	b.d.l	b.d.l	b.d.l	0.41	0.47	b.d.l	b.d.l	b.d.l	b.d.l	b.d.l	b.d.l	b.d.l
Al_2O_3	b.d.l	b.d.l			1.93	1.47	0.70	0.78	4.36	5.54	b.d.l	b.d.l	1.41	0.52	0.63	b.d.l	0.35
Y_2O_3	b.d.l	b.d.l			b.d.l	0.31	0.21	0.31	0.22	0.29	b.d.l	1.43	1.09	0.43	0.17	b.d.l	0.29
La_2O_3					0.32	b.d.l	b.d.l	0.42	0.23	0.173	b.d.l	b.d.l	0.55	0.64	0.28	b.d.l	b.d.l
Ce_2O_3					1.13	1.26	0.80	0.96	0.61	0.49	b.d.l	b.d.l	1.74	3.97	0.91	b.d.l	1.41
Nd_2O_3					0.99	0.80	0.68	b.d.l	0.41	0.23	b.d.l	b.d.l	1.41	3.00	b.d.l	b.d.l	1.33
Sc_2O_3					b.d.l	0.06	b.d.l	b.d.l	b.d.l	b.d.l	b.d.l	b.d.l	b.d.l	b.d.l	0.10	b.d.l	b.d.l
P_2O_5					4.48	b.d.l	b.d.l	b.d.l	b.d.l	b.d.l	b.d.l	0.26	9.39	4.65	0.70	0.29	0.86
FeO	b.d.l	b.d.l	b.d.l		1.75	2.20	0.90	1.26	5.65	8.35	0.14	b.d.l	1.98	2.86	2.12	0.23	2.49
CaO	b.d.l	b.d.l	b.d.l		0.77	3.29	1.18	1.58	1.76	1.66	2.18	b.d.l	1.50	0.81	2.44	3.10	1.04
F	0.30	0.28	0.35	0.31	0.38	0.37	0.36	0.42	0.46	0.38	0.51	0.34	0.56	0.74	0.36	1.97	0.87
Total	100.2	100.4	101.5	100.4	93.0	86.8	94.1	90.4	84.2	86.5	99.3	98.7	93.4	94.4	88.8	93.6	87.9
Mineral formulae (apfu)																	
Si	0.998	0.998	1.001	1.009	0.785	0.876	0.996	0.984			0.996	1.030	0.526	0.742	0.888	0.972	0.998
Zr	0.987	0.989	0.974	0.977	0.902	0.918	0.912	0.901			0.040	0	0.171	0.007	0.318	0	0
U	0	0	0	0.002	0.003	0.008	0.007	0.007			0.226	0.281	0.010	0.128	0.017	0.136	0.028
Th	0	0	0	0	0.003	0.004	0.005	0.008			0.674	0.644	0.594	0.629	0.576	0.775	0.765
Hf	0.015	0.013	0.025	0.012	0.011	0.018	0.010	0.011			0	0	0	0	0	0	0
Ti	0				0.018	0	0	0			0	0	0.051	0	0	0	0
Al	0	0	0	0	0.076	0.065	0.027	0.032			0	0	0.062	0.033	0.038	0	0.024
Y	0	0	0	0	0	0.006	0.004	0.006			0	0.040	0	0.012	0.005	0	0.009
La					0.004	0	0	0.005			0		0.010	0.013	0.005	0	0
Ce					0.014	0.017	0.010	0.012			0	0	0.031	0.078	0.017	0	0.029
Nd					0.012	0.011	0.008	0			0	0	0.024	0.057	0	0	0.027
Sc					0	0.002	0	0			0	0	0	0	0.004	0	0
P	0				0.127	0	0	0			0	0.011	0.380	0.210	0.030	0.014	0.041
Fe	0	0	0	0	0.049	0.069	0.025	0.037			0.006	0	0.079	0.128	0.091	0.011	0.118
Ca	0	0	0	0	0.028	0.132	0.042	0.059			0.122	0	0.077	0.046	0.133	0.189	0.063
F	0.029	0.027	0.034	0.030	0.041	0.043	0.038	0.046			0.085	0.057	0.085	0.125	0.058	0.353	0.156

Table 4 (continued)

Mineral	Mnz I	Mnz I	Mnz II	Mnz II	Mnz III	Mnz III	Ttn I	Ttn I	Ttn II	Ttn II	Ttn III	Ttn III	Allanite	Allanite	Allanite	Allanite
Sample	PET	PET	PET	PET	PET	PET	V-MEZ	SLA	POC	POC	PET	V-MEZ	POC[e]	SLA[e]	POC[f]	SLA[f]
Description	Bright	Bright	Dark	Dark	Bright	Bright	Bright	Dark	Bright	Bright	After bt	After bt	Bright	Bright	Dark	Dark
Major oxides (wt%)																
SiO_2	5.79	3.32	2.71	2.59	0.57	0.78	30.62	30.44	30.19	29.44	31.26	32.33	31.32	31.53	29.38	33.69
ZrO_2	b.d.l	b.d.l	3.14	2.06	b.d.l	b.d.l							3.02	1.66	5.32	3.17
TiO_2							35.84	37.37	34.93	35.37	28.70	26.95	b.d.l	b.d.l	0.12	0.38
UO_2	0.83	0.68	0.38	0.26	b.d.l	b.d.l							b.d.l	b.d.l	0.12	0.38
ThO_2	24.63	13.43	18.05	14.38	1.43	1.90							0.68	1.16	1.86	2.68
SnO_2							0.29	0.55	1.91	2.65	b.d.l	b.d.l				
Al_2O_3							1.44	1.38	1.50	1.18	6.84	8.76	14.93	14.54	13.88	14.01
La_2O_3	14.02	18.73	11.89	14.87	19.82	21.14	1.11	0.71	0.80	0.75	b.d.l	0.18	6.55	7.06	5.38	5.55
Ce_2O_3	23.20	28.41	20.84	20.14	34.41	34.48	0.79	0.49	0.63	0.53	b.d.l	b.d.l	11.58	11.74	9.93	9.95
Pr_2O_3	1.93	2.26	1.74	2.04	2.88	2.92							0.77	0.66	0.43	0.16
Nd_2O_3	7.33	7.18	4.02	5.06	8.96	7.82	0.33	0.23	0.42	0.42	b.d.l	b.d.l	3.05	2.77	2.52	1.95
Sm_2O_3	0.54	0.57	b.d.l	b.d.l	0.83	0.61							b.d.l	0.21	0.25	0.19
Gd_2O_3	b.d.l	b.d.l	b.d.l	b.d.l	0.35	0.18										
Y_2O_3	0.187	0.153	b.d.l	b.d.l	b.d.l	b.d.l	0.44	b.d.l	b.d.l	0.42	b.d.l	b.d.l	b.d.l	0.29	0.11	0.88
V_2O_3										b.d.l	0.47	b.d.l				b.d.l
P_2O_5	22.74	25.10	23.02	24.79	29.49	29.15					0.12	0.12	0.13	b.d.l	0.31	
Nb_2O_5							1.25	0.69	1.30	1.24		0.58				
As_2O_5	b.d.l	b.d.l	0.14	0.11	b.d.l	0.25										
FeO	b.d.l	0.45	0.49	1.19	0.29	0.44	0.39	0.34	0.47	0.30	1.86	0.58	11.38	7.95	10.40	7.49
CaO	0.51	0.33	6.56	6.26	0.45	0.35	27.95	28.34	27.67	27.27	27.52	29.28	9.02	10.60	7.14	8.03
MgO									b.d.l		1.39	0.07	1.34	1.55	0.87	1.01
MnO							b.d.l		b.d.l	0.06	b.d.l	b.d.l	0.38	0.57	0.49	0.79
PbO	0.47	0.22	0.49	0.62	0.55	0.25							0.22	b.d.l	0.38	0.44
SrO	b.d.l	b.d.l	0.52	0.46												
SO_3	b.d.l	b.d.l	0.46	0.31												
F	b.d.l	b.d.l	0.40	0.33			0.29	0.34	0.29	0.35	2.11	2.86	0.09	0.34	0.19	0.39
Total	102.2	100.8	94.3	95.0	100.0	100.3	100.7	100.9	100.1	99.6	100.3	101.1	94.5	92.6	88.9	90.8
Mineral formulae (apfu)																
Si	0.237	0.135	0.112	0.104	0.022	0.031	1.011	1.000	1.008	0.993	1.031	1.057	3.065	3.150	3.029	3.344
Zr	0	0	0.0630	0.0404	0	0							0.222	0.125	0.413	0.237
Ti							0.890	0.923	0.877	0.898	0.712	0.663		0	0.003	0.008
U	0.008	0.006	0.004	0.002	0	0							0	0	0.003	0.008
Th	0.229	0.124	0.169	0.132	0.013	0.017							0.015	0.026	0.044	0.061

Table 4 (continued)

	Pristine apatite					Uraninite			REE-fluorocarbonate			
Sample	PET	POC	TRE	V-MEZ	SLA	TRE	TRE	TRE	PET	TRE	V-MEZ	SLA
Description									Bright	Dark	Bright	Dark
Sn						0.004	0.007	0.025	1.721	1.711	1.687	1.638
Al	0.211	0.281	0.181	0.221	0.286	0.056	0.054	0.059	0.236	0.260	0.205	0.203
La	0.347	0.423	0.314	0.297	0.494	0.013	0.009	0.010	0.266	0.338	0.415	0.361
Ce	0.029	0.033	0.026	0.030	0.041	0.009	0.006	0.009	0.973	1.026	0.429	0.375
Pr	0.107	0.104	0.059	0.073	0.109	0.006	0.006	0.006	0.069		0.024	0.016
Nd	0.008	0.008		0	0.125	0.004	0.007		0		0.099	0.069
Sm	0	0	0	0	0.008	0.012	0	0	0.013	0	0.007	0.009
Gd	0.004	0.003	0.0005	0	0.002	0.019	0.020	0.019	0.002	0.002	0.016	0.006
Y	0.787	0.864	0.803	0.844	0	0.011	0.009	0.008	0.051	0.016	0	0.047
V					0.966	0.989	0.997	0.990	0.973	1.026		0
P	0.022	0	0.003	0.002	0.005	0	0	0	0.069	0.003	0	0.027
Nb	0	0.015	0.017	0.040	0.014	0	0	0	0	0	0.231	0.621
As	0.005	0.002	0.005	0.013	0.015	0.002	0	0.002	0	0.006	0.048	0.854
Fe	0	0	0.013	0.011	0.006						0	0.150
Ca	0	0	0.014	0.009	0	0.030	0.035	0.037	0.220	0.296	0.107	0.067
Mg	0	0	0.052	0.042	0					0.029	0.063	0.012
Mn												0.123
F												

Mineral	Pristine apatite					Uraninite			REE-fluorocarbonate			
Sample	PET	POC	TRE	V-MEZ	SLA	TRE	TRE	TRE	PET	TRE	V-MEZ	SLA
Description									Bright	Dark	Bright	Dark
Major oxides (wt%)												
SiO₂	0.33	0.27	0.22	0.32	0.33							
UO₂						82.63	82.60	84.26	b.d.l	b.d.l	b.d.l	b.d.l
ThO₂						10.70	10.75	9.39	1.19	1.29		1.80
La₂O₃	0.12	0.15	0.15	b.d.l	b.d.l	b.d.l	b.d.l	b.d.l	16.97	15.02	26.57	15.77
Ce₂O₃	0.22	0.33	0.36	0.35	0.24	0.59	0.64	0.40	27.66	24.00	31.53	27.87
Pr₂O₃									2.49	1.96	2.41	2.41
Nd₂O₃	b.d.l	b.d.l	b.d.l	0.32	0.21	0.86	0.38	0.83	7.33	5.75	5.70	7.42
Sm₂O₃									0.57	0.46	b.d.l	0.76
Gd₂O₃									b.d.l	b.d.l	b.d.l	b.d.l
Dy₂O₃						b.d.l		0.28				
Y₂O₃	b.d.l	b.d.l	b.d.l	0.16	b.d.l	0.85	0.83	0.62	0.32	0.38	b.d.l	0.39
P₂O₅	43.20	42.71	42.93	42.72	42.09							

Table 4 (continued)

FeO	0.31	0.40	0.75	1.30	0.24	0.29	0.15	0.22	b.d.l	0.21	b.d.l	b.d.l
CaO	12.62	4.56	17.28	12.17	0.07	b.d.l	0.07	55.29	54.99	55.14	55.34	54.38
MnO								0.07	0.08	0.09	0.06	0.09
PbO					4.05	4.04	3.96					
F	6.07	6.36	5.48	6.36				3.50	3.01	3.27	3.21	3.11
Cl								b.d.l	0.17	0.08	0.06	0.17
CO_2	25.06	21.59	27.36	25.06								
Total	100.5	99.1	100.3	100.9	100.1	99.5	99.8	101.9	102.1	102.5	102.1	101.6
Mineral formulae (apfu)												
Si	0	0	0	0				0.028	0.027	0.018	0.023	0.028
U	0	0	0	0	0.844	0.832	0.829					
Th	0.059	0.016	0.016	0.039	0.096	0.111	0.110					
La	0.838	0.404	0.307	0.902	0	0	0		0	0.005	0.005	0.004
Ce	1.469	0.476	0.487	1.460	0.007	0.011	0.010	0.007	0.011	0.011	0.010	0.007
Pr	0.127	0.036	0.040	0.130								
Nd	0.382	0.084	0.114	0.377	0.013	0.006	0.014	0.006	0.010			
Sm	0.038	0	0.009	0.028								
Gd	0	0	0	0								
Dy					0.004		0					
Y	0.030	0	0.011	0.025	0.015	0.020	0.020		0.007	0	0	0
P								2.980	3.003	3.010	3.002	3.035
Fe	0.038	0.014	0.060	0.091	0.009	0.011	0.006	0.016	0	0.015	0	0
Ca	1.947	0.202	1.026	1.879	0.003	0	0.003	4.955	4.892	4.894	4.923	4.836
Mn								0.005	0.005	0.007	0.005	0.006
Pb					0.049	0.049	0.048					
F	2.764	0.830	0.961	2.901				0.925	0.790	0.857	0.842	0.815
Cl								0	0.024	0.011	0.008	0.024
CO_3	4.926	1.215	2.071	4.931								

Cation proportions calculated based on a total of two (uraninite), four (zircon, thorite, monazite), five (titanite), and twelve (apatite, allanite) oxygen atoms per formula unit. The empirical formula of REE-fluorocarbonate calculated based on $\Sigma(REE+Y+U+Th+Ca^*)=1$ for synchisite and 3 for röntgenite. Ca^* is to balance Th and U charge which is higher compared to REEs. CO_2 in REE-fluorocarbonate calculated based on stoichiometry

TRE=Třebíč; PET=Petrůvky; POC=Pocoucov; V-MEZ=Velké Meziříčí; SLA=Slavkovice; b.d.l.=below detection limits; empty entries=not determined

[a] Zr-Th-U-Si-phase filling microveinlets surrounding altered zircon (see text for details)

[b] Preserved pristine U-rich thorite inclusions enclosed in zircon crystals

[c] Extensively altered thorite grains in the matrix

[d] Slightly altered thorite crystals in the matrix

[e] Less altered allanite domains

[f] Extensively altered allanite domains
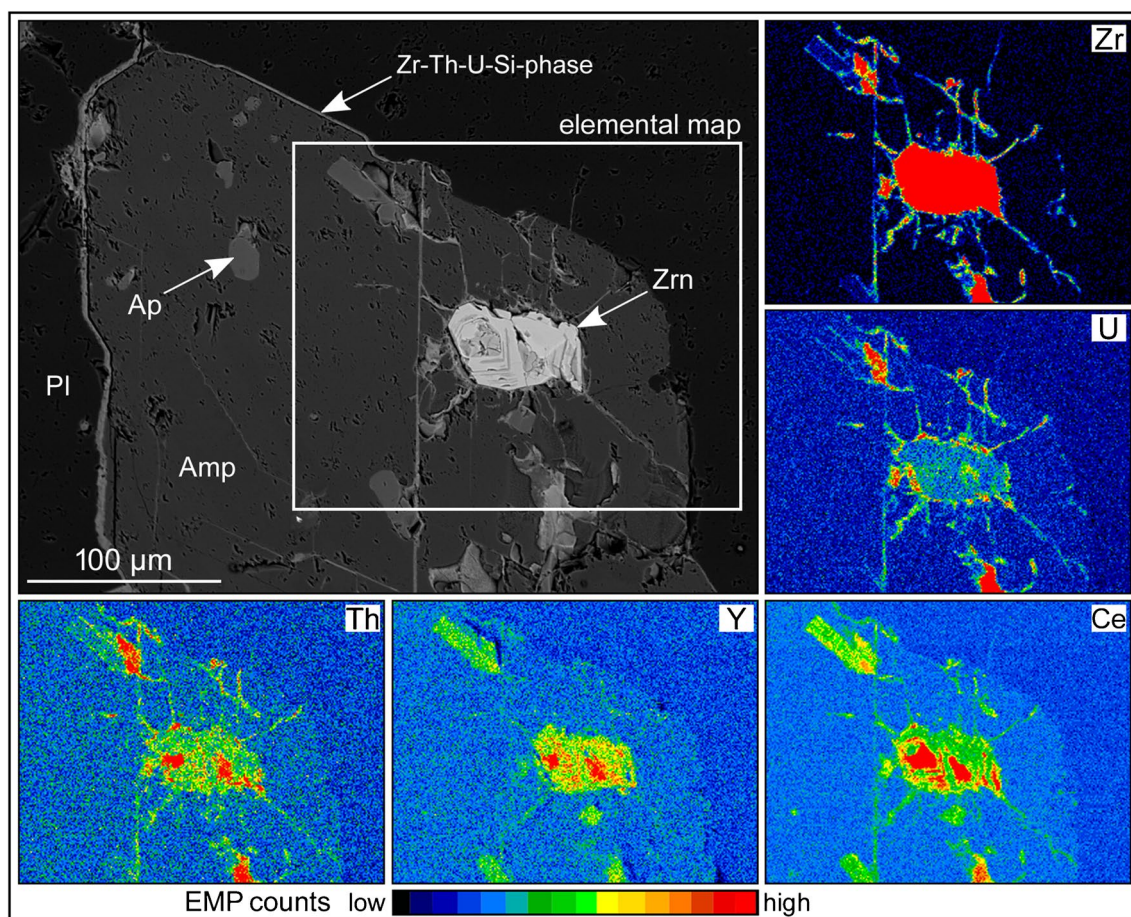
Fig. 9 BSE image and EMP elemental maps of partially altered zircon from ultrapotassic rocks. Note the resistance of apatite to fluid-driven alteration compared to hydrothermally decomposed zircon releasing Zr, Th, Y, and U. Abbreviations: Zrn = zircon, Ap = apatite, Amp = amphibole, Pl = plagioclase

crystals (25–70 μm) (Fig. 6e) that are usually intergrown with other primary accessory phases such as zircon or apatite. Its magmatic origin is indicated by textural features and high ThO_2 contents (8.14–10.75 wt%) (e.g., Cuney and Friedrich 1987; Förster 1999). Contents of UO_2 and PbO commonly vary between 82.60–85.20 wt% and 3.96–4.11 wt% (Table 4), respectively.

In addition, the EMP chemical dating of preserved magmatic uraninite grains provided age 337.9 ± 3.0 Ma (MSWD = 0.27) (ESM Table D), corresponding to the emplacement of the Třebíč durbachite intrusion, in line with the precise (CA-ID-TIMS) U–Pb zircon age of 335.127 ± 0.061 Ma previously obtained for the Třebíč pluton (Schaltegger et al. 2021).

Monazite-(Ce)

Three distinct monazite types with different textural features and chemistry occur in durbachite samples: pristine

magmatic Th-rich (Mnz I), altered magmatic (Mnz II), hydrothermal (Mnz III).

Mnz I was identified exclusively in samples from the PET where it occurs instead of U-rich thorite (Table 3) and forms subhedral grains (50–150 μm) showing a high intensity of alteration visible in BSE images (Fig. 6f). Mnz I exhibits high BSE intensity (Fig. 6f), EMP analytical totals (~ 100 wt%), and contents of REE_2O_3 (47.01–62.11 wt%) (especially LREE) and ThO_2 (10.47–24.63 wt%) along with low UO_2 (≤ 0.83 wt%) and CaO content (≤ 0.51 wt%).

Mnz II forms at expense of Mnz I, chemically resembles rhabdophane and shows lower BSE intensity (Fig. 6f), EMP analytical totals (92.2–95.7 wt%), decreased REE_2O_3 contents (34.75–42.11 wt%), and high ThO_2 (14.38–23.76 wt%) along with elevated CaO (≤ 6.87 wt%), ZrO_2 (up to 3.14 wt%), and F (up to 0.40 wt%) content.

Mnz III occurs as irregular crystals (10–160 μm) associated with REE-fluorocarbonate forming pseudomorphs after magmatic allanite (Fig. 7e) or independent aggregates set in the matrix (Fig. 7f). It usually shows relatively uniform

REE_2O_3 (65.66–69.10 wt%) content along with somewhat low ThO_2 (≤ 2.15 wt%) and UO_2 (≤ 0.08 wt%) concentrations (Table 4).

Titanite

Three distinct genetic types of titanite can be distinguished within the studied samples: early magmatic (Ttn I), late-magmatic (Ttn II), and hydrothermal (Ttn III).

Ttn I forms sub- to euhedral grains (100–750 μm) inter-grown with mafic silicates (Fig. 6g); occasionally, it occurs as euhedral crystals in the matrix. It commonly shows sectoral zonation and no visible effects of alteration (Fig. 6g). The chemistry of Ttn I is uniform among studied localities (Table 4), it mainly depends on different zonation patterns when BSE-brighter domains show slightly higher REE_2O_3 (e.g., Ce_2O_3 up to 1.11 wt%) and Nb_2O_5 (up to 1.59 wt%) content compared to BSE-darker domains ($Ce_2O_3 \leq 0.69$ wt%, $Nb_2O_5 \leq 0.54$ wt%).

Ttn II, observed solely in samples from the POC (Table 3), forms irregular grains (200–450 μm) with weak patchy zonation (Fig. 6g), enclosed in amphibole and K-feldspar in the matrix. The characteristic feature of Ttn II is notably high SnO_2 content reaching up to 2.68 wt%.

Ttn III replaces biotite and forms cleavage-oriented lenticular inclusions (< 90 μm) enclosed in cleavage cracks of chloritized biotite or irregular grains (10–180 μm) occurring in interstitial grain boundaries between altered biotite (Fig. 7d). Ttn III exhibits variable chemical composition within and between individual samples, particularly in case of F (0.35–2.86 wt%) and Al_2O_3 (1.14–8.76 wt%) (Table 4).

Allanite

Magmatic allanite occurs in samples from the POC and SLA as euhedral grains (300–1250 μm) with preserved primary sectoral zonation (Table 3). Note that allanite never coexists with primary Mnz I, reflecting a petrographic variability of common durbachite rocks. It usually encloses other accessory phases, mainly zircon and apatite. Allanite experienced a variable degree of late hydrothermal alteration, as suggested by patchy zonation in partially altered grains (Fig. 6h), the occurrence of almost entirely dissolved allanite crystals with low BSE intensity and high porosity (Fig. 6i) and the presence of pseudomorphs of REE-fluorocarbonate and Mnz III after allanite observed in common durbachite rocks (Fig. 7e).
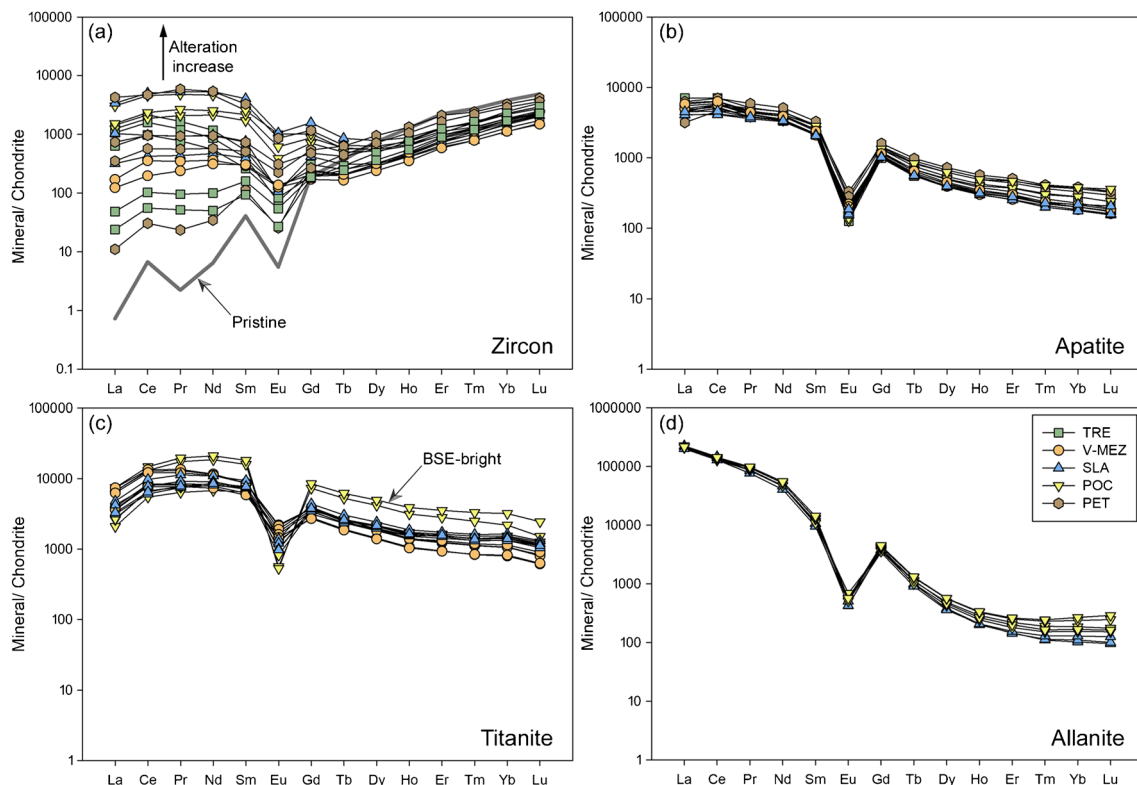
Fig. 10 a–d Chondrite-normalized (McDonough and Sun 1995) REE patterns of common accessory minerals in ultrapotassic rocks. REE pattern of rarely preserved pristine zircon is shown for comparison. REE composition of BSE-bright domains of early-magmatic titanite (Ttn I) is illustrated (see Fig. 6g). Abbreviations same as in Fig. 1

Table 5 LA-ICP-MS analyses (ppm) of accessory phases from ultrapotassic rocks

Mineral	Altered zircon					Pristine apatite					Pristine titanite					Altered allanite				
Sample	POC[a]	PET	TRE	V-MEZ	SLA	POC	PET	TRE	V-MEZ	SLA	POC[b]	POC[c]	V-MEZ[b]	V-MEZ[c]	SLA[c]	POC[b]	POC[c]	SLA[b]	SLA[c]	D.L.
Sc	517	481	509	393	385	0.32	0.27	0.38	2.1	0.21	26	20.7	11	17	14	103	113	82	114	0.2
Ga	0.06	0.31	0.31	3.1	34.1	23.6	29	26	24	15	83	66	62	44	47	502	571	579	550	0.04
Ge	0.70	1.3	2.3	3.2	36.9	20.5	27	23	20	14	104	81	65	49	55	226	272	247	253	0.1
Sr	0.89	0.73	1.4	1.7	9.0	166	370	213	278	201	5.9	4.49	27	21	14.3	579	470	1277	431	0.001
Y	2276	1758	1228	656	1699	740	870	616	505	411	5281	4309	2183	2143	2507	349	446	249	399	0.01
Zr	454,384	461,392	440,043	408,232	421,562	8.2	1.2	1.4	1.3	0.97	682	370	569	306	319	613	816	1826	963	0.01
Nb	2.79	5.0	3.5	7.1	25	0.07	b.d.l	0.061	0.569	0.024	14,324	3728	8343	2276	5053	3.6	4.6	4.2	5.4	0.01
La	0.172	2.6	5.7	40	809	1056	1492	1669	1374	775	1772	1022	1751	937	1001	49,926	51,238	53,343	51,364	0.01
Ce	4.13	19	34	218	3101	3491	4294	4343	3855	2203	9056	5776	8215	5133	4790	79,094	88,504	90,193	84,015	0.01
Pr	0.207	2.18	4.82	32.3	492	420	546	476	410	272	1824	1179	1253	781	848	8024	9161	7931	8794	0.02
Nd	2.96	15.8	22.9	166	2448	1882	2340	2046	1770	1161	9630	6242	5302	3770	4152	21,552	25,288	21,189	23,886	0.04
Sm	6.1	16.7	13.9	42.9	602	418	485	418	353	239	2692	1894	1273	1041	1091	1731	2117	1572	1938	0.01
Eu	0.3	1.4	1.5	7.1	60	7.2	16	9.4	11	8.7	30	20	120	90.7	68	31.3	31.8	24	28.8	0.02
Gd	38	53	36	34	315	266	320	264	228	159	1685	1198	745	681	688	753	894	752	841	0.02
Tb	13	16	11	6.0	31	30	35	27	23	16	223	162	89	85	85.1	40.3	47.6	35.8	46.4	0.01
Dy	185	177	120	59	193	153	179	134	110	79	1218	901	453	449	487	120	140	92.7	138	0.01
Ho	70	58	42	19	48.3	27	31	23	19	14	212	152	75	77	84	15.8	18.3	11	18	0.01
Er	356	264	200	94	206	75	81	60	48	37	568	398	197	211	249	35	42	24	40	0.01
Tm	68	54	41	20	37.9	9.94	10.2	7.7	5.9	4.66	81.6	54.1	27.7	29	35	4.7	6.0	2.7	5.7	0.01
Yb	610	467	366	181	352	61	62	45	35	29	515	318	172	184	239	30	43	17	38	0.01
Lu	120	89	73	37	68	8.9	8.2	5.8	4.6	4.15	60	35.1	20.2	22	30	4.3	7.1	2.4	6.1	0.01
Hf	11,486	15,040	11,908	12,892	11,720	0.50	b.d.l	b.d.l	0.11	b.d.l	147	56	36	20	64	13	25	17	26	0.01
Ta	1.1	3.33	2.14	2.55	4.78	0.015	b.d.l	b.d.l	b.d.l	b.d.l	3910	1074	231	80	1041	0.20	1.5	0.06	0.74	0.01
Pb	5.8	48	17	36	361	23	13	14	9.7	13.9	88	36	13	5.4	12	2578	2612	3309	3273	0.02
Th	141	1470	406	842	6961	58.6	82.4	127	74.2	68.7	132	77.3	186	88	101	23,393	17,650	15,416	19,881	0.01
U	367	4304	1815	2769	6786	79.8	185	121	105	66.7	170	166	260	150	179	756	780	1476	870	0.01
ΣREE	1474	1237	971	956	8763	7904	9900	9529	8247	5000	29,566	19,351	19,693	13,491	13,847	161,362	177,538	175,189	171,159	
La_N/Yb_N	0.00019	0.0038	0.011	0.15	1.56	11.78	16.45	25.08	26.98	18.34	2.34	2.18	6.92	3.46	285	1131	804	2196	911	
Eu_N/Eu_N^*	0.06	0.15	0.21	0.56	0.42	0.07	0.12	0.09	0.12	0.14	0.04	0.04	0.38	0.33	0.24	0.08	0.07	0.07	0.07	
Ce_N/Ce_N^*	5.30	1.89	1.58	1.46	1.19	1.17														

TRE = Třebíč; PET = Petrůvky; POC = Pocoucov; V-MEZ = Velké Meziříčí; SLA = Slavkovice; D.L. = detection limits; b.d.l. = below detection limits

[a] Chemical composition of the rarely preserved pristine zircon is given for comparison with altered zircon crystals (see text for details)

[b] BSE-brighter sector-zoned crystal domains

[c] BSE-darker sector-zoned crystal domains

The chemistry of allanite is highly variable because of pervasive fluid-driven alteration (Table 4). In general, less altered allanite domains tend to have the highest REE_2O_3 concentrations (up to 22.44 wt%), whereas partially altered grains with patchy zonation have relatively lower REE_2O_3 contents (17.20–20.31 wt%). Contents of UO_2 and ThO_2 range between 0.11–0.38 wt% and 0.68–2.98 wt%, respectively.

REE-fluorocarbonate

REE-fluorocarbonate is a typical hydrothermally-derived phase of secondary origin present in durbachite rocks. It occurs as irregular fine-grained aggregates (10–250 μm) forming pseudomorphs after magmatic allanite or independent grains in the matrix (Fig. 7e, f). In addition, REE-fluorocarbonate occurs as alteration haloes surrounding altered U-rich thorite and/or it fills cleavage plains of chloritized biotite enclosing altered thorite (Fig. 7b, c). The chemistry of REE-fluorocarbonate (synchisite–röntgenite) is relatively homogenous among durbachite samples, only with slight variations between BSE-brighter (REE_2O_3 56.65–69.67 wt%, CaO 1.85–12.17 wt%) and BSE-darker (REE_2O_3 43.54–54.23 wt%, CaO 12.62–19.07 wt%) domains of analyzed aggregates. Contents of ThO_2 (≤ 2.70 wt%) and F (4.58–7.39 wt%) are slightly variable (Table 4).

Trace elements in accessory minerals

Zircon

In this section, we provide data from zircon grains showing a variable degree of alteration, in line with BSE imaging and EMP analyses. Accordingly, one single analysis of rare unaltered pristine zircon is presented here to assess the modification of the trace element budget of zircon due to hydrothermal alteration (Fig. 10a, Table 5).

Altered zircon exhibits high and variable U, Th, Y, and $\sum REE$ contents ranging in hundreds to thousands of ppm, whereas Nb and Ta contents are somewhat low. Pristine zircon shows lower U and Th, higher Y, and similar $\sum REE$, Nb, and Ta contents relative to altered zircon (Table 5).

Altered zircon features lower HREE contents, variable LREE enrichment relative to HREE, less pronounced negative Eu ($Eu_N/Eu_N^* \sim 0.15$–0.63) anomaly and weak or no positive Ce ($Ce_N/Ce_N^* \sim 0.95$–1.89) anomaly compared to pristine zircon showing HREE-enriched patterns (Fig. 10a) with well-pronounced negative Eu and positive Ce anomaly ($Eu_N/Eu_N^* \sim 0.06$; $Ce_N/Ce_N^* \sim 5.30$), corresponding to the composition of magmatic zircon (Hoskin and Schaltegger 2003).

Apatite

Trace element chemistry of pristine apatite shows rather low U and Th contents, commonly in tens of ppm, although it

hosts relatively high amounts of REE, Y, and Sr (Table 5). Contents of other HFSE such as Zr, Nb, and Ta are negligible (Table 5).

Chondrite-normalized REE patterns (Fig. 10b) are fairly uniform among ultrapotassic plutons, with a typical LREE enrichment ($La_N/Yb_N \sim 11.78$–30.70) and strong negative Eu anomaly ($Eu_N/Eu_N^* \sim 0.06$–0.15).

Titanite

In this section, we present chemistry of pristine Ttn I which incorporates significant amounts of REE + Y and some HFSE, particularly Nb and Ta (Table 5). Trace element chemistry of Ttn I is uniform among ultrapotassic plutons, but it differs between distinct BSE domains within analyzed grains (Fig. 6g). The BSE-brighter domains exhibit higher trace element contents (e.g., REE $\leq 29,600$ ppm, Nb $\leq 14,300$ ppm, Ta ≤ 3910 ppm) compared to BSE-darker domains (REE $\leq 17,000$, Nb ≤ 5600 ppm, $\leq$ Ta 1120 ppm) (Fig. 10c).

Chondrite-normalized REE patterns are similar among ultrapotassic plutons, having a convex-upward trend ($La_N/Yb_N \sim 1.53$–6.92) with pronounced negative Eu anomaly ($Eu_N/Eu_N^* \sim 0.04$–0.44) (Fig. 10c).

Allanite

Trace element chemistry of partially altered magmatic allanite is provided in this section (Fig. 10d). Allanite represents the major carrier of LREE in ultrapotassic rocks (Table 5). It contains relatively high U and Th concentrations reaching up to thousands and ten thousand of ppm, respectively. Notably, allanite shows variable $\sum REE$, U, Th, and Zr contents (Table 5) even within a single BSE domain of the analyzed grain.

Overall, chondrite-normalized REE patterns (Fig. 10d) show strong LREE enrichment ($La_N/Yb_N \sim 2200$) relative to HREE and well-marked negative Eu anomaly ($Eu_N/Eu_N^* \sim 0.07$–0.11).

Whole-rock geochemistry

The studied samples span a wide range in major and minor element compositions (Fig. 11a, Table 6). The durbachite rocks show relatively variable SiO_2 (54.91–66.18 wt%) and MgO (2.90–7.06 wt%) contents along with high K_2O (6.04–7.01 wt%) contents. According to classification diagram in Fig. 11a (Middlemost 1994), the plutons are composed of monzonites (PET, V-MEZ) to quartz monzonites (POC, TRE, SLA). All samples fall in the shoshonitic field (Fig. 11b) within the SiO_2 vs. K_2O diagram (Peccerillo and Taylor 1976). The durbachites typically display metaluminous composition (A/CNK 0.79–0.90; molar $Al_2O_3/$
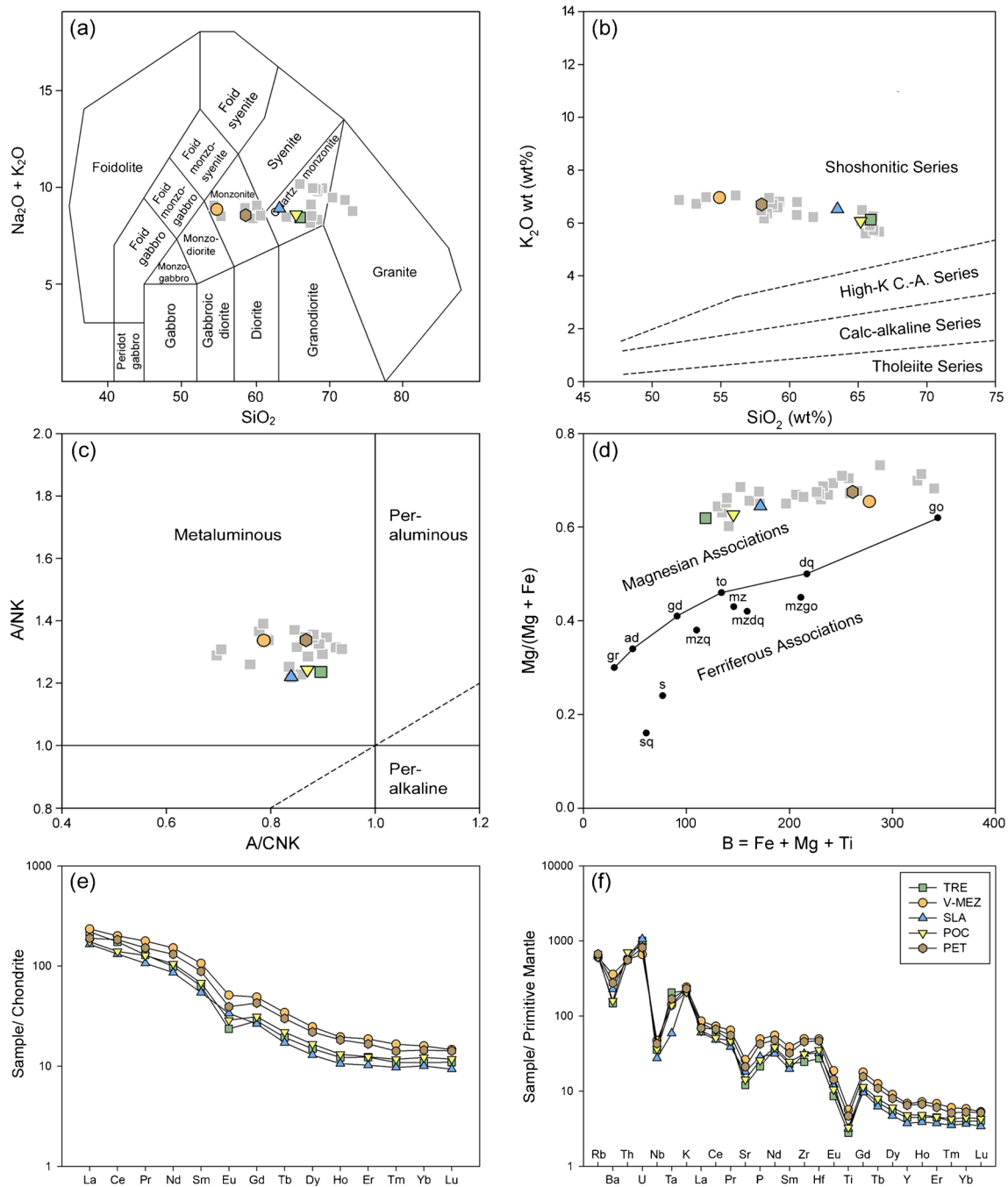
Fig. 11 Whole-rock geochemistry of ultrapotassic rocks. **a** Binary plot SiO$_2$ vs. Na$_2$O + K$_2$O (Middlemost [1994]), **b** SiO$_2$ vs. K$_2$O (Peccerillo and Taylor [1976]), **c** A/CNK vs. A/NK (Shand [1943]), **d** multicationic plot B vs. Mg# (Debon and Le Fort [1988]). **e** Chondrite-normalized REE patterns and **f** primitive-mantle-normalized multielement spider plot, standardized values are from McDonough and Sun ([1995]). Abbreviations same as in Fig. 1. Grey symbols for ultrapotassic rocks from the Trebíc pluton from Janoušek et al. ([2020])

[CaO + K$_2$O + Na$_2$O]) (Fig. 11c; Shand [1943]) together with highly magnesian character (Fig. 11d) (Debon and Le Fort [1988]).

The durbachite plutons are characterized by notably high U and Th contents ranging between 13.4–21.5 and 44.2–56.2 ppm (Table 6), respectively. All

samples feature LREE-enriched patterns (La$_N$/Yb$_N$ 13.09–20.15) with weak negative Eu anomalies (Eu$_N$/Eu$_N$* ~ 0.56–0.89) (Fig. 11e). Primitive mantle-normalized (McDonough and Sun [1995]) extended trace element patterns display strong enrichment in Th, U, Rb, Ba, and K (Fig. 11f).

Table 6 Whole-rock major (wt%) and trace element (ppm) composition of ultrapotassic rocks

Sample	TRE	PET	POC	V-MEZ	SLA	D.L
SiO_2	66.18	57.9	65.73	54.91	63.41	0.01
TiO_2	0.56	0.94	0.66	1.14	0.64	0.01
Al_2O_3	12.86	13.96	13.3	14.19	13.54	0.01
Cr_2O_3	0.027	0.065	0.033	0.065	0.038	0.002
FeO_{tot}	3.14	5.85	3.72	6.45	4.18	0.04
MgO	2.9	6.84	3.58	7.06	4.41	0.01
CaO	2.17	3.11	2.52	4.08	2.77	0.01
MnO	0.05	0.09	0.06	0.09	0.07	0.01
Na_2O	2.2	1.92	2.53	1.84	2.37	0.01
K_2O	6.27	6.72	6.04	7.01	6.65	0.01
P_2O_5	0.44	0.88	0.53	1.02	0.59	0.01
LOI	2.9	1.2	1	1.6	0.9	
Total	99.8	99.8	99.8	99.7	99.8	
Sr	241	421	284	522	362	0.5
Rb	391	402	364	365	372	0.1
Ba	972	1820	1054	2372	1508	1
Cs	18.1	30.6	45.8	17.2	34.2	0.1
Ga	17.7	20	17.8	19.7	18.2	0.5
Th	44.9	44.2	56.2	45.3	48.8	0.2
U	20.4	16.6	17.3	13.4	21.5	0.1
Ta	2.8	2.3	1.9	1.9	0.8	0.1
Nb	23.5	28.3	24	31.1	18.1	0.1
Zr	257	479	327	522	330	0.1
Hf	7.7	13.2	10	14	9.1	0.1
Y	19.1	28	20.7	29.5	16.1	0.1
Co	11.3	21.1	15.2	23.8	16.4	0.2
Sc	9	16	11	20	12	0.1
Ni	54	133	50	97	81	0.1
V	58	94	63	116	76	1
La	51.9	44.9	41.4	55.5	39	0.1
Ce	107	112	85.6	123	80.8	0.1
Pr	12	14.1	11.83	16.47	9.88	0.02
Nd	45.2	59.9	48.1	69.3	39.3	0.3
Sm	9.36	13.11	10.03	15.74	8.03	0.05
Eu	1.33	2.21	1.62	2.88	1.9	0.02
Gd	5.64	8.5	6.22	9.74	5.26	0.05
Tb	0.7	1.08	0.79	1.24	0.62	0.01
Dy	3.68	5.4	4.09	6.07	3.18	0.05
Ho	0.67	1	0.72	1.07	0.58	0.02
Er	1.97	2.67	1.99	2.99	1.64	0.03
Tm	0.27	0.35	0.29	0.41	0.24	0.01
Yb	1.75	2.33	1.97	2.57	1.62	0.05
Lu	0.27	0.35	0.29	0.36	0.23	0.01
$\sum$REE	242	268	215	307	192	
La_N/Yb_N	20.15	13.09	14.28	14.67	16.35	
Eu_N/Eu_N	0.56	0.64	0.63	0.71	0.89	

TRE = Třebíč; PET = Petrůvky; POC = Pocoucov; V-MEZ = Velké Meziříčí; SLA = Slavkovice; LOI = loss on ignition; D.L. = detection limits; FeO_{tot} = total iron oxide content
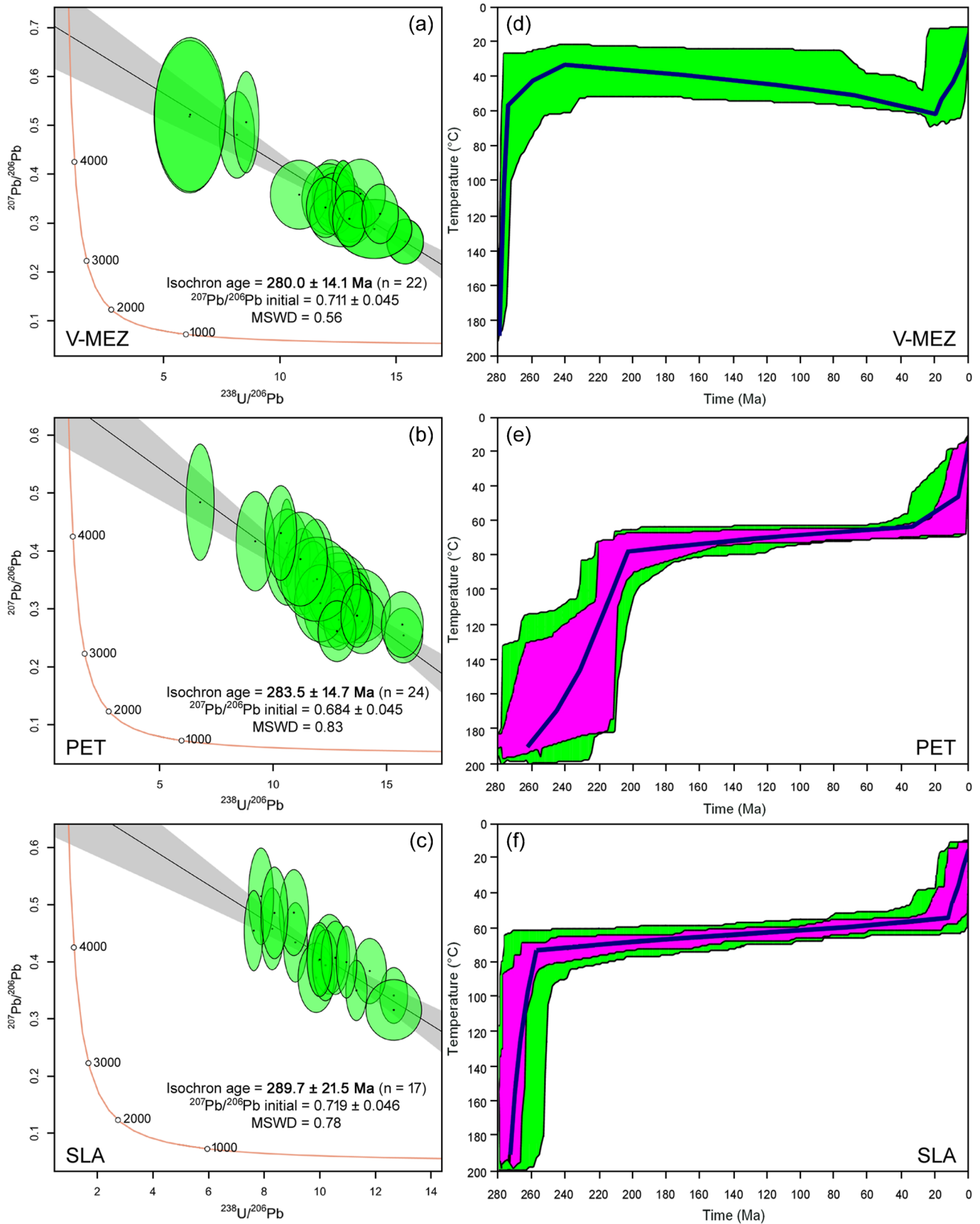
Fig. 12 **a–c** Tera-Wasserburg concordia diagrams displaying results of U–Pb apatite dating acquired for ultrapotassic plutons. **d–f** Apatite fission track (AFT) time–temperature history models of durbachite intrusions. Abbreviations same as in Fig. 1

Fig. 13 Airborne radiometric map showing Th/U ratios of the Třebíč durbachite pluton and surrounding metamorphic complexes that host numerous ore deposits of the Western Moravian U-province. Notice black dashed arrows highlighting NW–SE oriented zones, parallel to major fault systems in the Gföhl Unit, characterized by variously high Th/U values indicating U depletion (leaching)
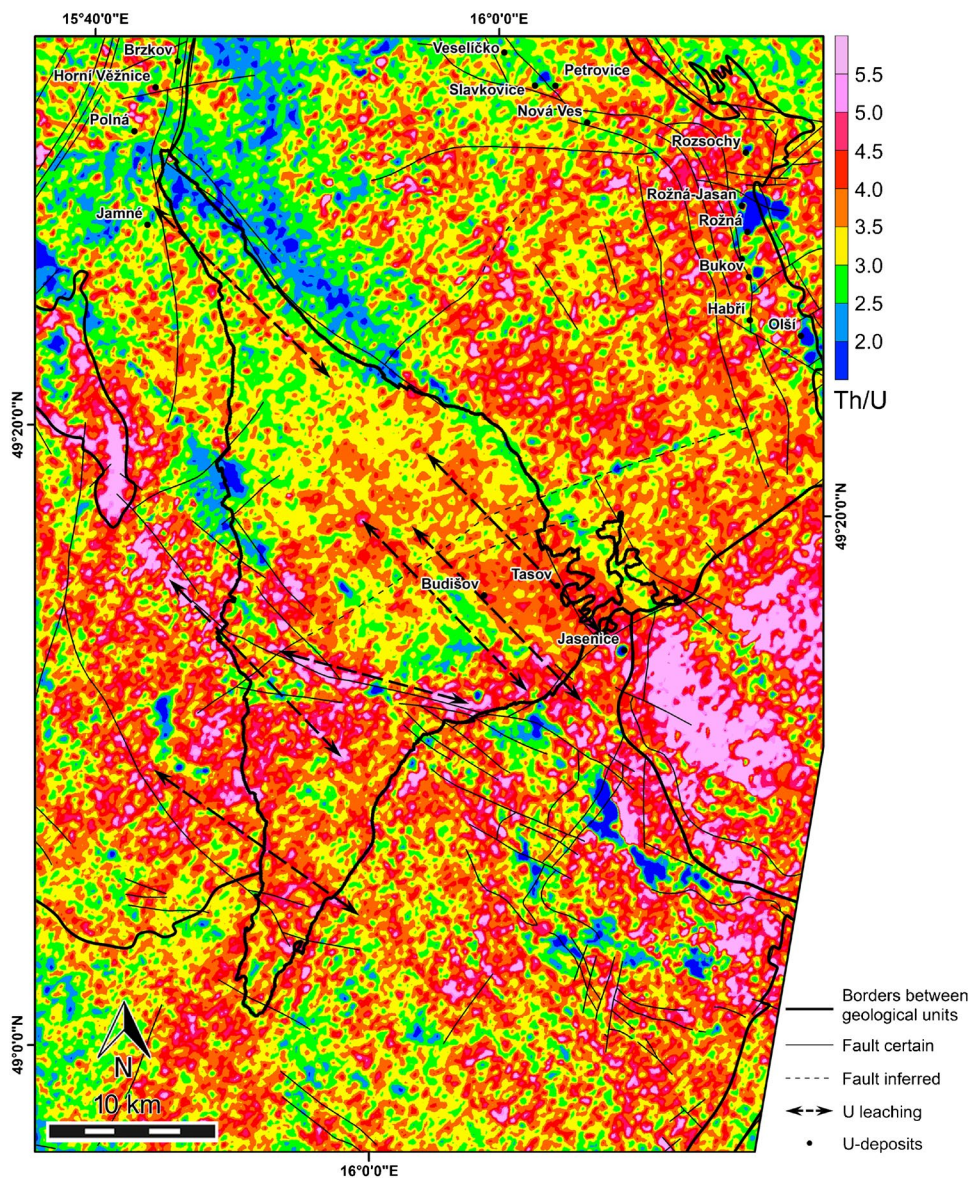
U–Pb apatite dating

Apatite has not experienced pervasive late alteration, and thus it represents an ideal phase for dating the (post-) magmatic evolution of durbachites. U–Pb apatite dating was performed on two samples from the Třebíč pluton (V-MEZ, PET) and one sample from its satellite body near Nové Město na Moravě (SLA) (Fig. 12a–c). Contents of U and Th in analyzed grains vary between 5.1–305.6 ppm and 2.5–213.5 ppm, with U/Th values of 0.68–4.41 (ESM Table E). Dated apatite fractions yield well-defined isochron dates in a range of 280–290 Ma (Fig. 12a–c) (V-MEZ ~ 280.0 ± 14.1 Ma with MSWD of 0.56; PET ~ 283.5 ± 14.7 Ma with MSWD of 0.83; SLA ~ 289.7 ± 21.5 Ma with MSWD of 0.78), corresponding

to a cooling age of ultrapotassic plutons (see Kubeš et al. 2022b for details).

Apatite fission-track (AFT) thermochronology

The results of the AFT analyses performed on the same samples used for the U–Pb apatite dating (V-MEZ, PET, SLA) are presented in ESM Table F. AFT ages are quoted as central ages (Galbraith and Laslett 1993) with ± 1σ uncertainties. The three durbachite samples from the localities V-MEZ, PET and SLA yield relatively variable central AFT ages of 246 ± 13 Ma, 172 ± 7 Ma and 210 ± 9 Ma, respectively. All samples have similar mean track lengths and D$_{par}$ values, varying between 11.64–12.43 μm and 1.72–2.26 μm, respectively. In addition, the AFT results from each sample were used to model the low-temperature thermal history of the durbachite plutons using the

HeFTy software (Fig. 12d–f) (Ketcham 2005). AFT thermal history models of durbachites are similar among individual samples, showing a rapid Permian uplift followed by stagnation until ca. 20 Ma (Fig. 12d–f). Note that the subsequent younger uplift lasting until the Holocene merely represents software artefacts inherent to HeFTy software, having no geological meaning (see Suchý et al. 2022 for details).

Airborne gamma-ray spectrometry

Ultrapotassic rocks of the Třebíč pluton show highly variable Th/U ratios varying between 1.5 and 6.0 (Fig. 13). The lowest Th/U values are typical for the NW corner of the Třebíč pluton, mainly reflecting the lithological variability of durbachites along with occurrences of granitic dykes and enclaves of metamorphic rocks (Leichmann et al. 2017). By contrast, the central part of the Třebíč pluton along with its southernmost corner features relatively high Th/U ratios (Fig. 13). Within the central part, the highest Th/U values notably line the W-E oriented Třebíč fault. Furthermore, the airborne radiometric map revealed a few km wide NW–SE oriented zones across the Třebíč pluton and surrounding metamorphic complexes characterized by elevated Th/U ratios that are parallel to the major fault zones developed in the Gföhl Unit (Figs. 1b and 13). Also, note that the high-grade metamorphic basement formed by anatectic gneisses and migmatites in the vicinity of the studied U-deposits show relatively low and less variable Th/U ratios compared to the Třebíč durbachitic pluton (Fig. 13).

Admittedly, some variations in Th/U ratios can be partially disturbed by the presence of surficial materials such as valley sediments or variations in the thickness of the soil cover. Also, the observed variability of major accessory phases controlling the distribution of radiogenic elements in the host durbachites can partially affect the airborne radiometric results. However, the recognition of NW–SE oriented zones parallel to prevailing fault systems points towards tectonically controlled U mobilization as a major mechanism responsible for these elevated Th/U ratios in the airborne radiometric map. By contrast, the subordinate NE-SW oriented fault zones across the Třebíč pluton do not manifest in the Th/U radiometric map (Fig. 13), probably suggesting that episodic faulting could not release stored radiogenic material from the host rocks.

Discussion

Anomalous trace element signatures of the U-deposits

The studied Moldanubian U-deposits are characterized by significant HFSE enrichment (Zr, Y, Nb, Ti) (Table 1

and 2), unusual for vein-type U-mineralization formed at low-temperature conditions (ca. 150–170 °C; see Kříbek et al. 2009). In general, the strong HFSE enrichment is commonly attributed to magmatic-related processes in the deposit formation (Alexandre et al. 2015). Thus, high Zr, Nb, and Ti are usually associated with high-temperature granite- and pegmatite-related U-deposits (Fig. 3c, d) (Frimmel et al. 2014). In addition, the notably high $\sum$REE content typical of uraninite from the Brzkov deposit (up to 1.12 wt%; Table 2) along with conspicuous HREE enrichment of the Rozsochy deposit (Fig. 4a) should also indicate a high temperature of ore crystallization, according to Fryer and Taylor (1987) and Pagel et al. (1987). However, the similar mineralogical paragenesis and textural features of the studied U-mineralization (Fig. 2a–d), characteristic of low-temperature shear zone-hosted U veins (Dahlkamp 2016; Kříbek et al. 2009), rule out the high-temperature uraninite crystallization as an important mechanism responsible for the anomalous HFSE and REE signatures.

Alternatively, the post-crystallization alteration and dissolution–precipitation processes may substantially affect the trace element distribution in uraninite (Martz et al. 2019a), as previously described for the hydrothermal vein-type U-deposit from Marshall Pass in Colorado (Fig. 3c, d) (Deditius et al. 2007). Nevertheless, EMP distribution maps (Fig. 2e–i) and analyses of pristine uraninite ($SiO_2 \leq 3.48$ wt%) (Fig. 3b) preclude the influence of post-crystallization alteration processes, except for Nb partially redistributed due to coffinitization (Fig. 2f, i).

Notably, the trace element signatures of the Moldanubian U-deposits are similar to those of the Proterozoic unconformity-related U-deposits from the Northern Territories in Australia (Fig. 3c, d) (Corcoran et al. 2019; references therein), suggesting a contribution of mineralizing fluids able to transport of HFSE along with REE over relatively long distances (e.g., Fayek and Kyser 1997; Mercadier et al. 2011b; Walsh and Spandler 2023). The highly variable chondrite-normalized REE patterns of the studied U-deposits (Fig. 4a–c) most likely reflect a contribution of different metal sources, similar to other significant hydrothermal U-deposits such as the Xianshi and Baishuizhai deposits from the North Guangdong Province in China (Bonnetti et al. 2018) and the Jáchymov deposit in the Czech Republic showing REE signatures typical of vein-type (Jáchymov I; Frimmel et al. 2014) as well as intrusive-related U-deposits (Fig. 4b, c) (Jáchymov II; Corcoran et al. 2019).

Based on all abovementioned observations, we conclude that a combination of other factors involving fluid chemistry and element availability in the source region must have controlled the anomalous trace element fingerprints of the Moldanubian U-mineralization, as will be discussed in detail within the following sections.

Deciphering the potential U source

Despite the presence of many U-deposits in the Moldanubian Zone of the Bohemian Massif (Fig. 1b), there is a lack of evidence for a direct genetic relationship between U-mineralization and U-fertile granitic rocks (Dahlkamp 2016), apart from a few deposits (e.g., Okrouhlá-Radoň, Zadní Chodov, Lhota) closely associated with granitic plutons (Dolníček et al. 2014; René 2017). Therefore, the high-grade metamorphic complexes hosting the Moldanubian U-deposits are currently considered as the most likely U source, related to hydrothermal decomposition of U-bearing accessories (Kříbek et al. 2009). Nevertheless, the airborne radiometric map presented in the current study (Fig. 13) demonstrates that the host rocks of the deposits cannot account for the main U source, with regard to their usually low and uniform Th/U ratios signalizing that U leaching during fluid-rock interaction has not occurred (e.g., Ballouard et al. 2018; Bonnetti et al. 2017). Moreover, the last metamorphic event recorded by the $^{40}Ar/^{39}Ar$ ages of the Moldanubian nappe assembly (325–331 Ma; Dallmeyer et al. 1992) preceded the formation of the studied vein-type U-deposits (U–Pb uraninite ~ 270 Ma; Fig. 5a), which precludes the possibility of the significant release of radiogenic elements with increasing metamorphic grade (e.g., Hasterok et al. 2018). In this section, we successively discuss a spatial, geochemical and genetic link between the vein-type U-deposits and ultrapotassic plutons of the durbachite series.

Spatial relation between the U-deposits and ultrapotassic intrusions

Based on surface radiometric survey and borehole logging carried out during U exploration in the Western Moravian U-province (Benedikt 1992; Chmelař and Chmelař 1992; Hlisnikovský 1993; Ondřík 1998), numerous occurrences of U-mineralization were documented within and nearby the Třebíč pluton and its smaller satellite bodies in the vicinity of cities Náměšť nad Oslavou, Drahonín and Nové Město na Moravě. As shown in Fig. 1c, the Brzkov deposit along with other relatively small U-deposits (e.g. Horní Věžnice, Polná, Jamné) are located a few km from the northernmost margin of the Třebíč pluton, which is typically lined with numerous radiometric U anomalies (up to 600 ppm U_{ekv}), reflecting the presence of U-mineralization, as further documented by borehole logging in the vicinity of the durbachitic intrusion (Ondřík 1998). The close spatial relation between the Jasenice deposit (Fig. 1b), which also hosts the U-Th-Zr mineralization previously described by Chmelař and Chmelař (1992), and the highly alkaline Naloučany intrusion near the Náměšť nad Oslavou

is confirmed by several boreholes and radiometric survey (see Kubeš et al. 2021 for details). The larger U-deposits Olší and Slavkovice-Petrovice are spatially associated with durbachite bodies nearby Drahonín and Nové Město na Moravě (Fig. 1b), also surrounded by numerous radiometric U anomalies in a range of 30–600 ppm U_{ekv} (Benedikt 1992). Furthermore, the occurrence of U-mineralization was described directly within the Třebíč pluton, nearby the Tasov and Budišov village (Fig. 1b), which is typically bounded to prevailing NW–SE-trending fault zones within the Gföhl Unit (Hlisnikovský 1993). Most importantly, it should be noted that the Třebíč pluton was originally about twice larger than today and its marginal parts reached the tectonic boundary between the Moldanubian Zone and the Svratka Complex (Fig. 1b), as previously estimated based on geophysical and petrological data (Leichmann et al. 2017), where most Moldanubian U-deposits are located (Dahlkamp 2016; Kříbek et al. 2009).

U-fertility of ultrapotassic rocks

The U-fertility of igneous rocks is mainly dependent on species of major U-bearing phases in the host rocks controlled by magma geochemistry (Cuney and Friedrich 1987; Wolf and London 1994). Therefore, U-fertile granitoids host a significant proportion of their U budget in uraninite or minerals that readily become metamict (e.g., thorite, zircon, allanite), enabling U redistribution from the source (Cuney 2009; Cuney and Kyser 2015; Yang et al. 2014).

The ultrapotassic plutons of the durbachite series geochemically corresponds to metaluminous to slightly peraluminous A2-type granites (Fig. 11a–d) (according to Eby 1992) with a significant enrichment in incompatible elements such as K, Rb, U, Th, and Zr (Fig. 11f; Table 6). However, it is noteworthy that strong U and Th enrichment of durbachites relates to low-degree partial melting of the crustally enriched lithospheric mantle (Kubeš et al. 2022b), without prolonged subsequent differentiation processes combined with a high degree of magma fractionation typical of common high-K calc-alkaline metaluminous igneous rocks (Cuney 2014). Instead, the relatively high SiO_2 content of ultrapotassic rocks (Table 6) most likely reflects the AFC-style crustal contamination by felsic anatectic melts, which also led to a slight decrease of K_2O, Rb, Ba, Th, and U contents typical of strongly contaminated marginal facies of the Třebíč pluton (Janoušek et al. 2020). The characteristic high U content of durbachites (13.4–21.5 ppm) with relatively low Th/U ratios (≤ 3.4) indicates crystallization of magmatic uraninite (Bonnetti et al. 2022; Chen et al. 2012; Förster 1999), easily leachable by oxidizing fluids. Indeed, primary uraninite was rarely observed in some durbachite samples (Fig. 6e). The high ThO_2 content in uraninite (≤ 10.75 wt%)

reflects its equilibrium crystallization with U-rich thorite (Cuney and Friedrich 1987) and the high crystallization temperature of ultrapotassic magmas (Kotková et al. 2010). Accordingly, U-rich thorite is a common phase in durbachites (Fig. 6c, d; Table 3) that may represent an important U source only if it becomes metamict in order to liberate U during infiltration of hydrothermal fluids, implying a time span of several 10 Ma between the magmatic crystallization and when U is significantly available for leaching (Bonnetti et al. 2017; Zhang et al. 2022). Considering a time interval between emplacement of durbachites (EMP U–Pb uraninite age ~ 338 Ma in this study; CA-ID-TIMS U–Pb zircon age ~ 335 Ma in Schaltegger et al. 2021) and U mobilization (SIMS U–Pb uraninite age ~ 270 Ma), a time gap of ~ 65 Ma is sufficient for accumulation of radiation damage in U-rich thorite and other U-bearing phases such as zircon and allanite (Fig. 6a, b, h, i), as suggested by temporal link between 20 and 50 Ma younger U-mineralization and emplacement of U-fertile granites in the European Variscides (Ballouard et al. 2018; Cathelineau et al. 2004; Kříbek et al. 1999, 2009; Romer and Cuney 2018).

From this follows that ultrapotassic rocks of the durbachite series in the Moldanubian Zone account for an ideal U source, with regard to their high whole-rock U content mainly stored in easily leachable uraninite and other refractory minerals (thorite, zircon, allanite) that became metamict at the time of hydrothermal fluid circulation, as further documented by EMP imaging and analyses of the main U-bearing phases.

Leaching of U and other metals

As revealed by the airborne radiometric map (Fig. 13), durbachites show notably variable Th/U values in contrast to metamorphic complexes hosting the U-deposits, which can be attributed to a combination between (1) crystallization of magmatic uraninite, (2) hydrothermal alteration, and (3) leaching and mobilization of U along fault zones, as previously demonstrated for U-fertile leucogranites in the Armorican Massif (Ballouard et al. 2018). Accordingly, a few km wide NW–SE oriented zones with elevated Th/U ratios, passing through the Třebíč pluton to surrounding lithologies (Fig. 13), suggest a large-scale U leaching along these zones that are typically parallel to major fault systems in the Gföhl Unit (Fig. 1b). As stated above, numerous occurrences of U-mineralization were documented along the NW–SE-trending faults within and nearby the Třebíč pluton during the previous radiometric survey (e.g., Hlisnikovský 1993). By contrast, the airborne radiometric map shows no visible variations of Th/U ratios associated with the subordinate NE-SW oriented faults across the Třebíč pluton (Fig. 13), which argues against the release of stored

radiogenic material from the host rocks during episodic faulting.

Such extensive U leaching from durbachites is in accordance with EMP analyses and imaging of their main U-bearing phases, recording massive mobilization of U along with HFSE and REE during fluid-rock interaction. Despite extensive fluid-driven decomposition of primary phases in durbachites, some accessory minerals retained their original magmatic textures that must be considered before assessing alteration-related trace element variations in major HFSE and REE carriers. For instance, abundant zircon usually features oscillatory zoning indicative of complex magma evolution (Kotková et al. 2010), which is typically underlined by lower BSE intensity (Fig. 6a, b) due to hydrothermal alteration, as suggested by Ce and Y enrichment typical of BSE-darker crystal domains of altered zircon (Fig. 9). Admittedly, the highly variable LREE enrichment of altered zircon grains (Fig. 10a), likely reflecting the intensity of hydrothermal alteration (see below), could be partially influenced by occurrences of micro- to submicroscopic inclusions (Zhong et al. 2018). Less altered allanite crystals preserved sectoral zonation, which is probably related to the rapid cooling and limited fractionation processes of ultrapotassic melts (Janoušek et al. 2020; Kubeš et al. 2022b), as further documented by variably LREE-enriched crystal domains of early-magmatic Ttn I (Figs. 6g and 10c). By contrast, rare Ttn II with a characteristic patchy zonation pattern (Fig. 6g; Table 3) presumably documents a late-stage magma evolution, considering its unusually high SnO_2 contents (up to 2.68 wt%), a typical feature of late-magmatic titanite (e.g., Xie et al. 2010).

U-rich thorite, abundant U host in the ultrapotassic plutons, experienced metamictization due to high initial U content and subsequent fluid-driven alteration, suggested by low BSE intensity (Fig. 6d), low EMP analytical totals, variable ThO_2 and UO_2 contents (Table 3 and 4), and association with REE-fluorocarbonate (Fig. 7a–c). Extensively altered BSE-darker thorite domains usually show lower UO_2 and ThO_2 contents than those the less altered BSE-brighter thorite domains (Fig. 6d), indicating that the U along with Th has been leached (Zhang et al. 2022). Considering different UO_2 content between pristine U-rich thorite enclosed in zircon (up to 30 wt%) (Cuney and Friedrich 1987) and altered thorite in the matrix (0.44–15.71 wt%), a significant U amount must have been leached during fluid-rock interaction. Furthermore, the presence of rarely preserved magmatic uraninite in durbachites (Fig. 6e; Table 3) indicates that most uraninite was probably leached by percolation of oxidizing fluids (Bonnetti et al. 2022; Tartèse et al. 2013; Wu et al. 2021). Accordingly, a mass-balance calculation revealed that ultrapotassic intrusions with the estimated original extent of 2000 km^3 (Leichmann et al. 2017) incorporated ca. 90×10^6 t U (calculated for a median

of 17.3 ppm U and density of 2.7 g/cm^3 of durbachites); such enormous initial U content was also estimated for the Variscan Questembert granites from the Armorican Massif (Tartèse et al. 2013). It implies that the volume of U mined from the Moldanubian deposits represents only a very small fraction of the amount of U present in ultrapotassic intrusions, considering a cumulative production of the Western Moravian U-province (~ 23,300 t U; Dahlkamp 2016). Other U-bearing accessories in durbachites such as zircon, allanite and monazite represent additional U hosts and may constitute the main REE source (Alexandre et al. 2015; Bonnetti et al. 2018; Hecht and Cuney 2000; Zhang et al. 2023), especially metamict zircon can release a significant HFSE and HREE amounts due to fluid-driven alteration (Kubeš et al. 2021; Walsh and Spandler 2023).

Zircon alteration manifests by Zr and Si depletion, enrichment in non-formula elements (Ca, Fe, Al, P) and Y, deficient EMP analytical totals (Fig. 8a, c, d) and low BSE intensity (Fig. 6a–c; Table 4) (Geisler et al. 2003; Kubeš et al. 2021; Zhang et al. 2020). Conspicuous U and Th enrichment in variably altered zircon crystals demonstrates interaction between zircon and U- and Th-bearing fluids (Fig. 8b). The extensive HFSE remobilization from altered zircon was controlled by interaction with hydrothermal fluids circulating through abundant microfractures formed by volume expansion due to zircon metamictization (Nasdala et al. 2010), as evidenced by the presence of Zr-Th-U-Si phase within these microfractures surrounding metamict zircon (Fig. 9). In contrast to rare pristine zircon, decreased HREE content of altered zircon, ordinarily showing variably LREE-enriched patterns with less pronounced positive Ce anomaly (Fig. 10a) (Borba et al. 2021), suggest extensive HREE leaching from zircon. Accordingly, HREE-enriched patterns with slight Ce anomaly typical of uraninite from the Rozsochy deposit (Fig. 4a) mimic the REE patterns of pristine zircon in durbachites (Fig. 10a), pointing to major REE source of the U-deposit (Mercadier et al. 2011a). The hydrothermal decomposition of zircon and subsequent long-distance mobilization of HREE along with Zr would explain anomalous HFSE enrichment of U-mineralization (Fig. 3c), a common feature of some Moldanubian U-deposits (Dolníček et al. 2014; Kříbek et al. 2009; René 2008; Wertich et al. 2022).

However, the studied U-deposits are characterized by variable REE signatures (Fig. 4a–c), likely reflecting different REE sources and/or mixing of ore-forming fluids with distinct chemistry. The Brzkov deposit features LREE-enriched pattern with weak Eu anomaly and unusually high ∑REE contents for low-temperature hydrothermal U-mineralization (Fig. 4c; Table 2) (Frimmel et al. 2014). Apart from apatite, showing no visible effects of dissolution (Fig. 6a), characteristic LREE-enriched

accessories in durbachites include allanite and monazite (Fig. 10d; Table 3 and 5), both of which experienced intensive hydrothermal decomposition (Fig. 6f, h, i) and replacement by secondary phases (Figs. 6f and 7e). Besides, a fluid-driven breakdown of titanite, previously observed in the Naloučany syenite body near the Třebíč pluton (Kubeš et al. 2021) and host metamorphic rocks of the U-deposits (Kříbek et al. 2022), can also liberate a significant amount of REE and other incompatible elements such as Nb and Ti typically reaching considerably high contents in the U-deposits (Fig. 3d; Table 2). With regard to notably high ∑REE content of uraninite from the Brzkov deposit, the contribution of more than one LREE-enriched source is likely. The flat REE pattern of the Rožná-Jasan deposit implies that hydrothermal fluids must have carried REE liberated during decomposition of two or more sources, probably including at least one HREE- and one LREE-dominated (zircon vs. allanite and/or monazite) (Fig. 10a, d; Table 3 and 5).

Conditions of large-scale fluid-driven HFSE and REE mobilization

The character of extensive post-magmatic alteration of primary accessory phases and mineral assemblages of hydrothermal phases in ultrapotassic plutons, in combination with trace element signatures of the U-deposits, provide crucial information about important chemical factors controlling the large-scale HFSE and REE mobility in hydrothermal systems.

The abundant occurrence of REE-fluorocarbonates in durbachite rocks (Fig. 7a–c; Table 3) indicates the influx of F- and CO_2-bearing fluids (Middleton et al. 2013). The formation of F-rich Ttn III after chloritized biotite (Fig. 7d) suggests that the major fluorine source was likely abundant biotite in ultrapotassic rocks, probably along with amphibole, both of which have released a significant fluorine amount due to chloritization, as evidenced by considerably low F content in partially to completely altered mafic silicates (ESM Table C). The infiltration of F-rich hydrothermal fluids is reflected by unusually high F content (up to 2.09 wt%) in extensively altered thorite and Mnz II (Table 4). Furthermore, elevated F content in Zr-Th-U-Si-phase (Table 4) typically associated with altered zircon (Fig. 9) suggests enhanced fluorine activity in fluids migrating through microveinlets formed by volume expansion due to zircon metamictization. The importance of fluoride as one of the principal complexing ligands in fluids is also demonstrated by extensive Th mobilization (Fig. 9) (Keppler and Wyllie 1990), increased solubility of monazite (Fig. 6f) (Tropper et al. 2013), and presence of secondary fluorite in strongly altered durbachites in close vicinity of the main faults crosscutting the Třebíč pluton

(Sulovský 2001). In accordance with the above-mentioned findings, the crucial role of fluorine in fluid-driven HFSE and REE mobilization was previously documented by observations from natural and experimental environments (e.g., Kubeš et al. 2021; Migdisov et al. 2011; Veksler 2004; Zeng et al. 2022).

Additionally, the presence of hydrothermal Mnz III in durbachites (Fig. 7e, f) indicates contribution of phosphate complexes in fluids, which may along with fluorine enhance HFSE and REE solubility (Migdisov et al. 2019). The influx of P-rich fluids is well-documented by variably high P_2O_5 contents in altered thorite (Table 4) and P_2O_5 enrichment (up to 4.53 wt%) in altered zircon typical for samples from the PET (Fig. 8a), which points to likely phosphorous source corresponding to partially dissolved Mnz I (Fig. 6f), exclusively observed in the PET. The hydrothermal destabilization of different sources (monazite vs. biotite ± amphibole) of P- and F-dominated complexing ligands, related to the petrographic variability of durbachites, was probably responsible for the variable fluid chemistry, providing an additional explanation for contrasting REE patterns of the U-deposits (Fig. 4a–c).

Importantly, the pervasive zircon dissolution and resistance of apatite to fluid-driven alteration in durbachites (Figs. 6a–c and 9) indicate alkaline conditions of the hydrothermal system since the Zr solubility ordinarily increases with high alkali content (pH > 10–12; Brendebach et al. 2007) whereas chemical solubility of apatite decreases with increasing pH; the measurement of dissolution rate of apatite is not possible for pH values greater than 8 (Guidry and Mackenzie 2003). From this follows that hydrothermal fluids, responsible for the dissolution of primary accessory phases in durbachites and subsequent HFSE and REE remobilization, probably evolved from Cl-rich basinal brines (see below) to highly alkaline F- and P-rich solutions due to interaction with durbachites. Indeed, the alkali-dominated REE complexes may represent important complexing ligands in hydrothermal fluids that allow REE mobilization (e.g., Veksler 2004). Moreover, potassic fluids preferentially transport HREE relative to sodic fluids and can migrate over long distances while retaining high REE solubilities, as revealed by experimental studies of carbonatite systems (Anenburg et al. 2020). Such preferential large-scale HREE mobilization is reflected by HREE-enriched patterns of the Rozsochy deposit (Fig. 4a), indicating the contribution of K-rich hydrothermal fluids in the deposit formation. Similar preferential fluid-driven HREE and HFSE liberation was also previously described in altered titanite from the Naloučany syenite near the Třebíč pluton (Kubeš et al. 2021), granitic rocks associated with regolith-hosted REE deposits in the Nanling Mountain Range (Dou et al. 2023) and pegmatite in southern Karnataka and Ontario (Pan et al. 1993). Accordingly, it was experimentally demonstrated that the capacity

for HFSE transporting by K- and F-bearing solutions is higher than that of Na- and F-bearing fluids (Zaraisky et al. 2010). Thus, the ability of fluids to transport HFSE along with REE became significantly high, as demonstrated by the chemistry of U-mineralization (Fig. 3c, d; Table 2), due to increased K contents of fluids by intensive chloritization of biotite in durbachites.

Likewise, the large-scale HFSE and REE mobilization has occurred at relatively low temperatures, recorded by chlorite thermometry (~270–300 °C; ESM Table C), in line with slightly lower temperatures estimated for formation conditions of the U-deposits (~150–170 °C; Kříbek et al. 2009) probably due to fluid-rock interaction and/or mixing of distinct types of fluids (Kříbek and Hájek 2005), and under oxidizing conditions with regard to dissolution of magmatic uraninite in durbachites and subsequent complexation of U in solutions (Xing et al. 2019). From this follows that low-temperature of hydrothermal system is not a limiting factor for the large-scale HFSE and REE remobilization, as documented by sandstone-hosted U–Zr-P-Ti-REE mineralization in the northern part of the Bohemian Cretaceous Basin (Mikysek et al. 2021).

Timing of U-mineralization and regional implications

The first in situ SIMS U–Pb age of 270.8 ± 7.5 Ma (Fig. 5a; ESM Table B) obtained so far for the U-mineralization from the Bohemian Massif provide constraints on the U metallogenetic model for the Moldanubian U-deposits in the Central European Variscides (Fig. 1a–c). The relatively low SiO_2 content (Fig. 3b; Table 1) in dated uraninite aggregates/domains and the concordance of some U–Pb analyses (Fig. 5a), implying only limited effects of post-crystallization alteration represented by coffinitization (Fig. 2a–f, 5b), indicate that the SIMS U–Pb uraninite date presented in the current study reflects the crystallization age of the U-mineralization. The Permian age of the Moldanubian U-deposits is in agreement with previous bulk-phase U–Pb (270–280 Ma; Anderson et al. 1988) and EMP U–Pb dating of uraninite (260–280 Ma; Wertich et al. 2022) from the Western Moravian U-province, K–Ar dates of illite from ore substage alteration (264–277 Ma; Kříbek et al. 2009) and U–Pb dates of authigenic monazite (~268 Ma; Kříbek et al. 2009) from the Rožná deposit.

The recognition that U mineralizing events occurred at ca. 270 Ma suggests that during the lithospheric extensional events, responsible for the coeval exhumation of the metamorphic complexes and the formation of the Late Carboniferous to Lower Permian sedimentary basins, the oxidizing surface- and basin-derived fluids (Kříbek et al. 2009) percolated through the crystalline basement and liberated U and other metals from the ultrapotassic rocks. The rapid Permian exhumation, recorded

by AFT thermal history models of durbachites (Fig. 12d–f), closely followed the cooling of ultrapotassic intrusions, reflected by U–Pb apatite ages (ca. 280–290 Ma) (Fig. 12a–c), and enabled the infiltration of oxidized Cl-rich basinal brines mixed with meteoritic waters that represent the most important ore-forming fluids in the entire European Variscan belt (Ballouard et al. 2017, 2018; Romer and Cuney 2018; Kříbek et al. 2009). The alkaline composition of oxidized basinal brines coupled with the high activity of F-, P-, and K-dominated complexing ligands, resulting from interaction with durbachites, indeed played an essential role in the large-scale HFSE and REE mobility related to the U-deposits formation. Assuming a much more extensive Permo-Carboniferous sedimentation, relative to the now preserved remnants (e.g., Boskovice and Jihlava furrow) (Fig. 1b), unconformably covering the high-grade metamorphic complexes of the eastern margin of the Moldanubian Zone (McCann et al. 2006), these U-deposits likely represent the basement rock-hosted part of the unconformity-type deposit, overlayed by Permian sedimentary cover that was nearly entirely eroded during the Mesozoic era. The unconformity-related origin of the Moldanubian U-deposits is further supported by the large-scale HFSE and REE mobility usually linked to the formation of this deposit type (Fayek and Kyser 1997; Frimmel et al. 2014; Gaboreau et al. 2007; Mercadier et al. 2011b; Walsh and Spandler 2023). Moreover, the significant modification of chemical composition of basin-derived fluids during the interaction with the basement-hosted ultrapotassic rocks (e.g., K and F release during biotite chloritization, P liberation through monazite alteration) led to the formation of mineralizing fluids and the genesis of significant ore deposits, such as the unconformity-related U-deposits (Martz et al. 2019b). Accordingly, the deep infiltration of oxidized basinal fluids into the crystalline basement is reflected by prominent hematitization, dequartzification, and albitization of the host metamorphic complexes along shear zones (Dahlkamp 2016; Kříbek et al. 2009).

On a larger continental scale, U deposition in the Moldanubian Zone of the Bohemian Massif was contemporaneous with U mineralizing events in the large metallogenic provinces within the Massif Central, Armorican Massif, Black Forest and Erzgebirge (Cathelineau et al. 1990; Förster and Haack 1995; Hofmann and Eikenberg 1991; Marignac and Cuney 1999; Velichkin and Vlasov 2011). Indeed, the Permian period hosts the main U mineralizing events in the European Variscides and most U deposits are genetically linked to Carboniferous U-fertile leucogranites (Ballouard et al. 2018; Cuney et al. 1990; Romer and Cuney 2018), characterized by high heat production due to their high content of radioactive elements, which can maintain the convection of surface-derived fluids at depth several Ma after their emplacement (Ballouard et al. 2017). A similar scenario is envisioned for the ultrapotassic rocks of the durbachite series in the Moldanubian Zone, also characterized by significant heat flux caused by a notably high abundance of

radioactive elements (Table 6), which similar to Carboniferous leucogranites represent U-fertile source rocks and their emplacement (EMP U–Pb uraninite age ~ 338 Ma in this study; CA-ID-TIMS U–Pb zircon age ~ 335 Ma in Schaltegger et al. 2021) postdates the main mineralization stage (SIMS U–Pb uraninite age ~ 270 Ma) (Fig. 5a). Therefore, with regard to extensive ultrapotassic magmatism in the entire European Variscan Belt (von Raumer et al. 2014), U-fertile durbachite rocks can be considered as a potential U source for future U exploration targeting economically important ore deposits in the Central and Western European Variscides.

Conclusions

Our study of hydrothermal vein-type U-deposits and ultrapotassic rocks of the durbachite series in the Moldanubian Zone of the Bohemian Massif provides the following conclusions:

- The anomalous trace element signatures ($Zr \leq 2.32$ wt%, $Nb \leq 0.53$ wt%, $Y \leq 0.40$ wt%, $Ti \leq 0.48$ wt%, $\sum REE \leq 1.12$ wt%) of the low-temperature hydrothermal U-mineralization suggest a genetic link to spatially associated HFSE- and REE-rich durbachite rocks.
- EMP elemental maps coupled with LA-ICP-MS analyses of the main refractory U-bearing phases in durbachites recorded extensive mobilization of U along with HFSE and REE, controlled by fluid-driven alteration of the radiation-damaged U-rich minerals. Moreover, the presence of magmatic uraninite rarely preserved in durbachites probably suggests that most uraninite was entirely leached during hydrothermal alteration of the host rocks.
- Therefore, durbachites represent an ideal source for the formation of U-deposits as their high U content (13.4–21.5 ppm) is mainly stored in magmatic uraninite, an easily leachable phase during oxidizing fluid circulation, and in other refractory minerals (e.g., thorite, zircon, allanite) that became metamict over a time interval sufficient to liberate U from their crystal structure.
- The large-scale HFSE and REE remobilization, recorded by unusual trace element signatures of the Moldanubian U-deposits, occurred under highly alkaline conditions due to infiltration of low-temperature aqueous solutions with F-, P-, and K-dominated complexing ligands.
- The SIMS uraninite U–Pb age of 270.8 ± 7.5 Ma for the Rozsochy deposit reveals a Permian U mineralization stage, related to crustal extensional events responsible for the coeval exhumation of the crystalline basement, recorded by U–Pb apatite ages (280–290 Ma) and AFT thermal history models of durbachites, and the formation of the Permo-Carboniferous sedimentary basins that

generated oxidized brines percolating through basement-hosted durbachite rocks and leaching a significant U amount.

- The significant modification of the chemical composition of basin-derived fluids during the interaction with durbachite rocks (e.g., F and K release during biotite chloritization, P liberation through monazite decomposition) resulted in the formation of alkaline ore-bearing fluids responsible for the large-scale HFSE and REE mobilization linked to the metallogenesis of the unconformity-related U-deposits on shear zones.

Declarations

Conflict of interest The authors declare no competing interests.

References

Alexandre P, Kyser K, Layton-Matthews D, Joy B, Uvarova Y (2015) Chemical compositions of natural uraninite. Can Mineral 53:595–622. https://doi.org/10.3749/canmin.1500017

Anderson EB, Ivanov PA, Komínek J (1988) Ore metasomatism at the uranium veins of the Rožná deposit. Geol Hydrometal Uranium 12:70–89 ((**in Czech with English summary**))

Anenburg M, Mavrogenes JA, Frigo C, Wall F (2020) Rare earth element mobility in and around carbonatites controlled by sodium, potassium, and silica. Sci Adv 6:1–10. https://doi.org/10.1126/sciadv.abb6570

Arapov JA, Bojcov VJ, Česnokov NI, Djakonov AV, Halbršťát J, Jakovjenko AM, Kolek M, Komínek J, Kozyrev VN, Kremčkukov GA, Lažanský M, Milovanov IA, Nový V, Šorf F (1984) Uranium deposits of the Czechoslovakia. Czechoslovak Uranium Industry, pp 420. (in Czech with English summary)

Balboni E, Jones N, Spano T, Simonetti A, Burns PC (2016) Chemical and Sr isotopic characterization of North America uranium ores: nuclear forensic applications. Appl Geochem 74:24–32. https://doi.org/10.1016/j.apgeochem.2016.08.016

Ballouard C, Poujol M, Boulvais P, Mercadier J, Tartèse R, Venneman T, Deloule E, Jolivet M, Kéré I, Cathelineau M, Cuney M (2017) Magmatic and hydrothermal behavior of uranium in syntectonic leucogranites: the uranium mineralization associated with the Hercynian Guérande granite (Armorican Massif, France). Ore Geol Rev 80:309–331. https://doi.org/10.1016/j.oregeorev.2016.06.034

Ballouard C, Poujol M, Mercadier J, Deloule E, Boulvais P, Baele JM, Cuney M, Cathelineau M (2018) Uranium metallogenesis of the peraluminous leucogranite from the Pontivy-Rostrenen magmatic complex (French Armorican Variscan belt): the result of long-term oxidized hydrothermal alteration during strike-slip deformation. Miner Deposita 53:601–628. https://doi.org/10.1007/s00126-017-0761-5

Benedikt Z (1992) Final report of the results of the borehole drilling survey in the Slavkovice Section. MS GEAM, Dolní Rožínka, pp 4 (in Czech)

Bonnetti C, Cuney M, Bourlange S, Deloule E, Poujol M, Liu X, Peng Y, Yang J (2017) Primary uranium sources for sedimentary-hosted uranium deposits in NE China: insight from basement igneous rocks of the Erlian Basin. Miner Deposita 52:297–315. https://doi.org/10.1007/s00126-016-0661-0

Bonnetti C, Liu X, Mercadier J, Cuney M, Deloule E, Villeneuve J, Liu W (2018) The genesis of granite-related hydrothermal uranium deposits in the Xiazhuang and Zhuguang ore fields, North Guangdong Province, SE China: Insights from mineralogical, trace elements and U-Pb isotopes signatures of the U mineralisation. Ore Geol Rev 92:588–612. https://doi.org/10.1016/j.oregeorev.2017.12.010

Bonnetti C, Riegler T, Liu X, Cuney M (2022) Granite-related high-temperature hydrothermal uranium mineralisation: evidence from the alteration fingerprint associated with an early Yanshanian magmatic event in the Nanling belt, SE China. Miner Deposita. https://doi.org/10.1007/s00126-022-01137-9

Borba ML, Tassinari CC, Matos FM, Sato K, Huhn S, Ferreira SN, Medeiros CA (2021) Tracking hydrothermal events using zircon REE geochemistry from the Carajás Mineral Province. Brazil J Geochem Explor 221:106679. https://doi.org/10.1016/j.gexplo.2020.106679

Brendebach B, Altmaier M, Rothe J, Neck V, Denecke MA (2007) EXAFS study of aqueous Zr^{IV} and Th^{IV} complexes in alkaline $CaCl_2$ solutions: $Ca_3[Zr(OH)_6]^{4+}$ and $Ca_4[Th(OH)_8]^{4+}$. Inorg Chem 46:6804–6810. https://doi.org/10.1021/ic070318t

Cathelineau M (1988) Cation site occupancy in chlorites and illites as a function of temperature. Clay Miner 23:471–485. https://doi.org/10.1180/claymin.1988.023.4.13

Cathelineau M, Boiron MC, Holliger P, Poty B (1990) Metallogenesis of the French part of the Variscan orogen. Part II: Time-space relationships between U, Au and Sn-W ore deposition and geodynamic events—mineralogical and U-Pb data. Tectonophysics 177:59–79. https://doi.org/10.1016/0040-1951(90)90274-C

Cathelineau M, Fourcade S, Clauer N, Buschaert S, Rousset D, Boiron MC, Meunier A, Lavastre V, Javoy M (2004) Dating multistage paleofluid percolations: a K-Ar and 18O/16O study of fracture illites from altered Hercynian plutonites at the basement/cover

interface (Poitou High, France). Geochim Cosmochim Acta 68:2529–2542. https://doi.org/10.1016/j.gca.2003.10.037

Chen YW, Bi XW, Hu RZ, Dong SH (2012) Element geochemistry, mineralogy, geochronology and zircon Hf isotope of the Luxi and Xiazhuang granites in Guangdong province, China: implications for U mineralization. Lithos 150:119–134. https://doi.org/10.1016/j.lithos.2012.06.025

Chew DM, Donelick RA, Sylvester P (2012) Combined apatite fission track and U-Pb dating by LA-ICP-MS and its application in apatite provenance analysis. Mineral Ass Canada Short Course 42:219–247

Chmelař J, Chmelař J (1992) Final report of the geological survey within the Naloučany Section – uranium deposit Jasenice. MS GEAM, Dolní Rožínka, pp 127 (in Czech)

Cooke RA, O'Brien PJ (2001) Resolving the relationship between high P-T rocks and gneisses in collisional terranes: an example from the Gföhl gneiss–granulite association in the Moldanubian Zone, Austria. Lithos 58:33–54. https://doi.org/10.1016/S0024-4937(01)00049-4

Corcoran L, Simonetti A, Spano TL, Lewis SR, Dorais C, Simonetti S, Burns PC (2019) Multivariate analysis based on geochemical, isotopic, and mineralogical compositions of uranium-rich samples. Minerals 9:537. https://doi.org/10.3390/min9090537

Cuney M (2009) The extreme diversity of uranium deposits. Miner Deposita 44:3–9. https://doi.org/10.1007/s00126-008-0223-1

Cuney M (2014) Felsic magmatism and uranium deposits. Bull Soc Géol France 185:75–92. https://doi.org/10.2113/gssgfbull.185.2.75

Cuney M, Friedrich M (1987) Physicochemical and crystal-chemical controls on accessory mineral paragenesis in granitoids: implications for uranium metallogenesis. Bull Mineral 110:235–247

Cuney M, Kyser K (2015) Geology and geochemistry of uranium and thorium deposits. Min Assoc Can 46:362

Cuney M, Friedrich M, Blumenfeld P, Bourguignon A, Boiron MC, Vigneresse JL, Poty B (1990) Metallogenesis in the French part of the Variscan orogen. Part I: U preconcentrations in pre-Variscan and Variscan formations—a comparison with Sn. W and Au Tectonophysics 177:39–57. https://doi.org/10.1016/0040-1951(90)90273-B

Dahlkamp FJ (2016) Uranium Deposits of the World: Europe. 1. In: Springer-Verlag, Berlin Heidelberg, pp 792. https://doi.org/10.1007/978-3-540-78554-5

Dallmeyer DR, Neubauer F, Höck V (1992) Chronology of late Paleozoic tectonothermal activity in the southeastern Bohemian massif, Austria (Moldanubian and Moravo-Silesian zone): ^{40}Ar/^{39}Ar mineral age controls. Tectonophysics 210:135–153. https://doi.org/10.1016/0040-1951(92)90132-P

Debon F, Le Fort P (1988) A cationic classification of common plutonic rocks and their magmatic associations: principles, method, applications. Bull Mineral 111:493–510

Deditius AP, Utsunomiya S, Ewing RC (2007) Fate of trace elements during alteration of uraninite in a hydrothermal vein-type U-deposit from Marshall Pass, Colorado, USA. Geochim Cosmochim Acta 71:4954–4973. https://doi.org/10.1016/j.gca.2007.08.008

Deloule E, Alexandrov P, Cheilletz A, Laumonier B, Barbey P (2002) In-situ U-Pb zircon ages for Early Ordovician magmatism in the eastern Pyrenees, France: the Canigou orthogneisses. Int J Earth Sci 91:398–405. https://doi.org/10.1007/s00531-001-0232-0

Depiné M, Frimmel HE, Emsbo P, Koenig AE, Kern M (2013) Trace element distribution in uraninite from Mesoarchean Witwatersrand conglomerates (South Africa) supports placer model and magmatogenic source. Miner Deposita 48:423–435. https://doi.org/10.1007/s00126-013-0458-3

Dolníček Z, René M, Hermannová S, Prochaska W (2014) Origin of the Okrouhlá Radouň episyenite-hosted uranium deposit, Bohemian Massif, Czech Republic: fluid inclusion and stable isotope constraints. Miner Deposita 49:409–425. https://doi.org/10.1007/s00126-013-0500-5

Donelick RA, O'Sullivan PB, Ketcham RA (2005) Apatite Fission-Track Analysis. Rev Mineral Geochem 58:49–94. https://doi.org/10.2138/rmg.2005.58.3

Dou J, Wang CY, Xing Y, Tan W, Zhao Z (2023) Redistribution of REE in granitic bedrocks during incipient weathering: insights into the role of groundwater in the formation of regolith-hosted REE deposit. Contrib Mineral Petrol 178:69. https://doi.org/10.1007/s00410-023-02054-4

Eby GN (1992) Chemical subdivision of the A-type granitoids: petrogenetic and tectonic implications. Geology 20:641–644. https://doi.org/10.1130/0091-7613(1992)020%3c0641:CSOTAT%3e2.3.CO;2

Faltusová V, Vaculovič T, Holá M, Kanický V (2022) Ilaps - python software for data reduction and imaging with LA-ICP-MS. J Anal at Spectrom 37:733–740. https://doi.org/10.1039/d1ja00383f

Fayek M, Kyser TK (1997) Characterization of multiple fluid-flow events and rare-earth-element mobility associated with formation of unconformity-type uranium deposits in the Athabasca Basin, Saskatchewan. Can Mineral 35:627–658

Finger F, Roberts MP, Haunschmid B, Schermaier A, Steyrer HP (1997) Variscan granitoids of central Europe: their typology, potential sources and tectonothermal relations. Mineral Petrol 61:67–96. https://doi.org/10.1007/bf01172478

Förster HJ (1999) The chemical composition of uraninite in Variscan granites of the Erzgebirge, Germany. Mineral Mag 63:239–252. https://doi.org/10.1180/002646199548466

Förster B, Haack U (1995) U/Pb-Datierungen von Pechblenden und die hydrothermale Entwicklung der U-Lagerstätte Aue-Niederschlema (Erzgebirge). Z Geol Wiss 23(5/6):581–588

Friedl G, Finger F, Paquette JL, von Quadt A, McNaughton NJ, Fletcher IR (2004) Pre-Variscan geological events in the Austrian part of the Bohemian Massif deduced from U-Pb zircon ages. Int J Earth Sci 93:802–823. https://doi.org/10.1007/s00531-004-0420-9

Frimmel HE, Schedel S, Brätz H (2014) Uraninite chemistry as forensic tool for provenance analysis. Appl Geochem 48:104–121. https://doi.org/10.1016/j.apgeochem.2014.07.013

Fryer BJ, Taylor RP (1987) Rare-earth element distributions in uraninites: implications for ore genesis. Chem Geol 63:101–108. https://doi.org/10.1016/0009-2541(87)90077-5

Gaboreau S, Cuney M, Quirt D, Beaufort D, Patrier P, Mathieu R (2007) Significance of aluminium phosphate-sulfate minerals associated with U unconformity-type deposits: the Athabasca basin, Canada. Am Mineral 92:267–280. https://doi.org/10.2138/am.2007.2277

Galbraith RF, Laslett GM (1993) Statistical models for mixed fission track ages. Nucl Tracks Rad Meas 21:459–470. https://doi.org/10.1016/1359-0189(93)90185-C

Geisler T, Pidgeon RT, Kurtz R, Van Bronswijk W, Schleicher H (2003) Experimental hydrothermal alteration of partially metamict zircon. Am Mineral 88:1496–1513. https://doi.org/10.2138/am-2003-1013

Guidry MW, Mackenzie FT (2003) Experimental study of igneous and sedimentary apatite dissolution: control of pH, distance from equilibrium, and temperature on dissolution rates. Geochim Cosmochim Acta 67:2949–2963. https://doi.org/10.1016/S0016-7037(03)00265-5

Hasterok D, Gard M, Webb J (2018) On the radiogenic heat production of metamorphic, igneous, and sedimentary rocks. Geosci Front 9:1777–1794. https://doi.org/10.1016/j.gsf.2017.10.012

Hecht L, Cuney M (2000) Hydrothermal alteration of monazite in the Precambrian crystalline basement of the Athabasca Basin (Saskatchewan, Canada): implications for the formation of unconformity-related uranium deposits. Miner Deposita 35:791–795. https://doi.org/10.1007/s001260050280

Hein U, Lehmann B, Křříbek B, René M (2002) Evolution of ore-forming fluids along the Rožná-Olší shear zone, Bohemian Massif, Czech Republic: implication for local uranium deposition and comparison with U-mineralization at Schlema, Erzgebirge, Germany. In: Křříbek B, Zeman J (eds) Uranium deposits: from their genesis to their environmental aspects, 1st edn. Czech Geological Survey, Prague, pp 61–64

Hlisnikovský K (1993) Final report of the uranium exploration within the Tasov Section. Manuscript, GEAM Dolní Rožínka (in Czech)

Hofmann B, Eikenberg J (1991) The Krunkelbach uranium deposit, Schwarzwald, Germany; correlation of radiometric ages (U-Pb, U-Xe-Kr, K-Ar, ^{230}Th-^{234}U). Econ Geol 86:1031–1049. https://doi.org/10.2113/gsecongeo.86.5.1031

Hoskin PW, Schaltegger U (2003) The composition of zircon and igneous and metamorphic petrogenesis. Rev Mineral Geochem 53:27–62. https://doi.org/10.2113/0530027

Janoušek V, Hanžl P, Svojtka M, Hora JM, Kochergina YVE, Gadas P, Holub FV, Gerdes A, Verner K, Hrdličková K, Daly JS (2020) Ultrapotassic magmatism in the heyday of the Variscan Orogeny: the story of the Třebíč Pluton, the largest durbachitic body in the Bohemian Massif. Int J Earth Sci 109:1767–1810. https://doi.org/10.1007/s00531-020-01872-2

Jowett E (1991) Fitting iron and magnesium into the hydrothermal chlorite geothermometer. Program Abstr 16:A62

Keppler H, Wyllie PJ (1990) Role of fluids in transport and fractionation of uranium and thorium in magmatic processes. Nature 348:531–533. https://doi.org/10.1038/348531a0

Ketcham RA (2005) Forward and inverse modeling of low-temperature thermochronometry data. Rev Mineral Geochem 58:275–314. https://doi.org/10.2138/rmg.2005.58.11

Košler J, Konopásek J, Sláma J, Vrána S (2014) U-Pb zircon provenance of Moldanubian metasediments in the Bohemian Massif. J Geol Soc 171:83–95. https://doi.org/10.1144/jgs2013-059

Kotková J, Schaltegger U, Leichmann J (2010) Two types of ultrapotassic plutonic rocks in the Bohemian Massif—Coeval intrusions at different crustal levels. Lithos 115:163–176. https://doi.org/10.1016/j.lithos.2009.11.016

Křříbek B, Hájek A (2005) The Rožná uranium deposit. Czech Geological Survey, Prague (in Czech with English summary)

Křříbek B, Žák K, Spangenberg JE, Jehlička J, Prokeš S, Komínek J (1999) Bitumens in the late Variscan hydrothermal vein-type uranium deposit of Pribram, Czech Republic; sources, radiation-induced alteration, and relation to mineralization. Econ Geol 94:1093–1114. https://doi.org/10.2113/gsecongeo.94.7.1093

Křříbek B, Žák K, Dobeš P, Leichmann J, Pudilová M, René M, Scharm B, Scharmová M, Hájek A, Holéczy D, Hein UF, Lehmann B (2009) The Rožná uranium deposit (Bohemian Massif, Czech Republic): shear zone-hosted, late Variscan and post-Variscan hydrothermal mineralization. Miner Deposita 44:99–128. https://doi.org/10.1007/s00126-008-0188-0

Křříbek B, Knésl I, Dobeš P, Veselovský F, Pořádek P, Škoda R, Čopjaková R, Leichmann J, Košek F (2022) The origin of synchysite-(Ce) and sources of rare earth elements in the Rožná uranium deposit. Czech Republic Minerals 12:690. https://doi.org/10.3390/min12060690

Kubeš M, Leichmann J, Wertich V, Mozola J, Holá M, Kanický V, Škoda R (2021) Metamictization and fluid-driven alteration triggering massive HFSE and REE mobilization from zircon and titanite: direct evidence from EMPA imaging and LA-ICP-MS analyses. Chem Geol 586:120593. https://doi.org/10.1016/j.chemgeo.2021.120593

Kubeš M, Leichman J, Kotková J, Čopjaková R, Holá M, Sláma J (2022a) Diversity of origin and geodynamic evolution of the mantle beneath the Variscan Orogen indicating rapid exhumation within subduction-related mélange (Moldanubian Zone, Bohemian Massif). Lithos 423:106726. https://doi.org/10.1016/j.lithos.2022.106726

Kubeš M, Leichmann J, Buriánek D, Holá M, Navrátil P, Scaillet S, O'Sullivan P (2022b) Highly evolved miaskitic syenites deciphering the origin and nature of enriched mantle source of ultrapotassic magmatism in the Variscan orogenic root (Bohemian Massif, Moldanubian Zone). Lithos 432:106890. https://doi.org/10.1016/j.lithos.2022.106890

Lardeaux JM, Schulmann K, Faure M, Janoušek V, Lexa O, Skrzypek E, Edel JB, Štípská P (2014) The Moldanubian zone in the French Massif Central, Vosges/Schwarzwald and Bohemian Massif revisited: differences and similarities. Geol Soc London, Spec Publ 405:7–44. https://doi.org/10.1144/SP405.14

Leichmann J, Gnojek I, Novák M, Sedlák J, Houzar S (2017) Durbachites from the Eastern Moldanubicum (Bohemian Massif): erosional relics of large, flat tabular intrusions of ultrapotassic melts–geophysical and petrological record. Int J Earth Sci 106:59–77. https://doi.org/10.1007/s00531-016-1296-1

Marignac C, Cuney M (1999) Ore deposits of the French Massif Central: insight into the metallogenesis of the Variscan collision belt. Miner Deposita 34:472–504. https://doi.org/10.1007/s001260050216

Martz P, Mercadier J, Perret J, Villeneuve J, Deloule E, Cathelineau M, Quirt D, Doney A, Ledru P (2019a) Post-crystallization alteration of natural uraninites: implications for dating, tracing, and nuclear forensics. Geochim Cosmochim Acta 249:138–159. https://doi.org/10.1016/j.gca.2019.01.025

Martz P, Mercadier J, Cathelineau M, Boiron MC, Quirt D, Doney A, Gerbeaud O, De Wally E, Ledru P (2019b) Formation of U-rich mineralizing fluids through basinal brine migration within basement-hosted shear zones: A large-scale study of the fluid chemistry around the unconformity-related Cigar Lake U deposit (Saskatchewan, Canada). Chem Geol 508:116–143. https://doi.org/10.1016/j.chemgeo.2018.05.042

Matte P, Maluski H, Rajlich P, Franke W (1990) Terrane boundaries in the Bohemian Massif: result of large-scale Variscan shearing. Tectonophysics 177:151–170. https://doi.org/10.1016/0040-1951(90)90279-H

McCann T, Pascal C, Timmerman M, Krzywiec P, López-Gómez J, Wetzel L, Krawczyk C, Rieke H, Lamarche J (2006) Post-Variscan (end Carboniferous-Early Permian) basin evolution in Western and Central Europe. Geological Society, London, Memoirs 32:355–388. https://doi.org/10.1144/gsl.mem.2006.032.01.22

McDonough W, Sun SS (1995) The composition of the Earth. Chem Geol 120:223–253. https://doi.org/10.1016/0009-2541(94)00140-4

McGloin MV, Tomkins AG, Webb GP, Spiers K, MacRae CM, Paterson D, Ryan CG (2015) Release of uranium from highly radiogenic zircon through metamictization: the source of orogenic uranium ores. Geology 44:15–18. https://doi.org/10.1130/G37238.1

Mercadier J, Cuney M, Lach P, Boiron MC, Bonhoure J, Richard A, Leisen M, Kister P (2011a) Origin of uranium deposits revealed by their rare earth element signature. Terra Nova 23:264–269. https://doi.org/10.1111/j.1365-3121.2011.01008.x

Mercadier J, Cuney M, Cathelineau M, Lacorde M (2011b) U redox fronts and kaolinisation in basement-hosted unconformity-related U ores of the Athabasca Basin (Canada): late U remobilisation by meteoric fluids. Miner Deposita 46:105–135. https://doi.org/10.1007/s00126-010-0314-7

Middlemost EA (1994) Naming materials in the magma/igneous rock system. Earth-Sci Rev 37:215–224. https://doi.org/10.1016/0012-8252(94)90029-9

Middleton AW, Förster HJ, Uysal IT, Golding SD, Rhede D (2013) Accessory phases from the Soultz monzogranite, Soultz-sous-Forêts, France: implications for titanite destabilisation and differential REE, Y and Th mobility in hydrothermal systems. Chem Geol 335:105–117. https://doi.org/10.1016/j.chemgeo.2012.10.047

Migdisov AA, Williams-Jones AE, Van Hinsberg V, Salvi S (2011) An experimental study of the solubility of baddeleyite (ZrO_2) in fluoride-bearing solutions at elevated temperature. Geochim Cosmochim Acta 75:7426–7434. https://doi.org/10.1016/j.gca.2011.09.043

Migdisov A, Guo X, Nisbet H, Xu H, Williams-Jones AE (2019) Fractionation of REE, U, and Th in natural ore-forming hydrothermal systems: thermodynamic modeling. J Chem Thermodyn 128:305–319. https://doi.org/10.1016/j.jct.2018.08.032

Mikysek P, Zikmund T, Dosbaba M, Břínek A, Slobodník M, Adamovič J, Mészárosová N, Trojek T, Kaiser J (2021) Multi-scale visualization of uranium-rich domains dispersed in U-Zr mineralization of sandstone-type (Břevniště, Czech Republic). Ore Geol Rev 138:104358. https://doi.org/10.1016/j.oregeorev.2021.104358

Moiny H, Faryad SW, Čopjaková R, Jedlička R (2020) Multi-stage metamorphism by progressive accretion of continental blocks, example from the Western Hindu Kush. J Metamorph Geol 38:693–717. https://doi.org/10.1111/jmg.12535

Nasdala L, Hanchar JM, Rhede D, Kennedy AK, Váczi T (2010) Retention of uranium in complexly altered zircon: An example from Bancroft, Ontario. Chem Geol 269:290–300. https://doi.org/10.1016/j.chemgeo.2009.10.004

O'Brien PJ, Rötzler J (2003) High-pressure granulites: formation, recovery of peak conditions and implications for tectonics. J Metamorph Geol 21:3–20. https://doi.org/10.1046/j.1525-1314.2003.00420.x

Ondřík J (1998) Final report of the uranium exploration within the Strážek Unit – South. Manuscript, GEAM Dolní Rožínka (in Czech)

Pagel M, Pinte G, Rotach-Toulhoat N (1987) The rare earth elements in natural uranium oxides. Monogr Ser Miner Dep 27:81–85

Pan YM, Fleet ME, MacRae ND (1993) Late alteration in titanite ($CaTiSiO_5$): redistribution and remobilization of rare earth elements and implications for U/Pb and Th/Pb geochronology and nuclear waste disposal. Geochim Cosmochim Acta 57:355–367. https://doi.org/10.1016/0016-7037(93)90437-2

Peccerillo A, Taylor SR (1976) Geochemistry of Eocene calc-alkaline volcanic rocks from the Kastamonu area, northern Turkey. Contrib Mineral Petrol 58:63–81. https://doi.org/10.1007/BF00384745

René M (2008) Anomalous rare earth element, yttrium and zirconium mobility associated with uranium mineralization. Terra Nova 20:52–58. https://doi.org/10.1111/j.1365-3121.2007.00786.x

René M (2017) Alteration of granitoids and crystalline rocks and uranium mineralisation in the Bor pluton area, Bohemian Massif, Czech Republic. Ore Geol Rev 81:188–200. https://doi.org/10.1016/j.oregeorev.2016.09.033

Romer RL, Cuney M (2018) Phanerozoic uranium mineralization in Variscan Europe–more than 400 Ma of tectonic, supergene, and climate-controlled uranium redistribution. Ore Geol Rev 102:474–504. https://doi.org/10.1016/j.oregeorev.2018.09.013

Schaltegger U, Gaynor SP, Widmann P, Kotková J (2021) Comment on "Ultrapotassic magmatism in the heyday of the Variscan Orogeny: the story of the Třebíč Pluton, the largest durbachitic body in the Bohemian Massif" by Janoušek et al. Int J Earth Sci 110:1127–1132. https://doi.org/10.1007/s00531-020-01975-w

Shand SJ (1943) Eruptive rocks. Their genesis, composition, classification, and their relation to ore-deposits with a chapter on meteorite, 2nd edn. Wiley, New York.

Stacey JT, Kramers JD (1975) Approximation of terrestrial lead isotope evolution by a two-stage model. Earth Planet Sci Lett 26:207–221. https://doi.org/10.1016/0012-821X(75)90088-6

Suchý V, Zachariáš J, Sýkorová I, Kořínková D, Pešek J, Brabcová KP, Luo Q, Filip J, Světlík I (2022) Palaeo-thermal history of the Blanice Graben (the Bohemian Massif, Czech Republic): the origin of anthracite in a late-Variscan strike-slip basin. Int J Coal Geol 263:104129. https://doi.org/10.1016/j.coal.2022.104129

Sulovský P (2001) Accessory minerals of the Třebíč durbachite massif (SW Moravia). Miner Slovaca 33:467–472

Tajčmanová L, Konopásek J, Schulmann K (2006) Thermal evolution of the orogenic lower crust during exhumation within a thickened Moldanubian root of the Variscan belt of Central Europe. J Metamorph Geol 24:119–134. https://doi.org/10.1111/j.1525-1314.2006.00629.x

Tartèse R, Boulvais P, Poujol M, Gloaguen E, Cuney M (2013) Uranium mobilization from the Variscan Questembert syntectonic granite during fluid-rock interaction at depth. Econ Geol 108:379–386. https://doi.org/10.2113/econgeo.108.2.379

Thomson SN, Gehrels GE, Ruiz J, Buchwaldt R (2012) Routine low-damage apatite U–Pb dating using laser ablation-multi-collector-ICPMS. Geochem Geophys Geosyst 13. https://doi.org/10.1029/2011GC003928

Timmerman MJ (2008) In: Palaeozoic magmatism. The Geology of Central Europe Volume 1: Precambrian and Palaeozoic, pp. 665–748. https://doi.org/10.1144/cev1p.12

Tropper P, Manning CE, Harlov DE (2013) Experimental determination of $CePO_4$ and YPO_4 solubilities in H_2O–NaF at 800 °C and 1 GPa: implications for rare earth element transport in high-grade metamorphic fluids. Geofluids 13:372–380. https://doi.org/10.1111/gfl.12031

Veksler IV (2004) Liquid immiscibility and its role at the magmatic–hydrothermal transition: a summary of experimental studies. Chem Geol 210:7–31. https://doi.org/10.1016/j.chemgeo.2004.06.002

Velichkin VI, Vlasov BP (2011) Domal structures and hydrothermal uranium deposits of the Erzgebirge, Saxony, Germany. Geol Ore Depos 53:74–83. https://doi.org/10.1134/S1075701511010053

von Raumer JF, Finger F, Veselá P, Stampfli GM (2014) Durbachites–Vaugnerites–a geodynamic marker in the central European Variscan orogen. Terra Nova 26:85–95. https://doi.org/10.1111/ter.12071

Walsh JM, Spandler C (2023) The role of zircon in hydrothermal heavy REE mineralisation: The case for unconformity-related ore deposits of north-west Australia. Chem Geol 629:121493. https://doi.org/10.1016/j.chemgeo.2023.121493

Wertich V, Kubeš M, Leichmann J, Holá M, Haifler J, Mozola J, Hršelová P, Jaroš M (2022) Trace element signatures of uraninite controlled by fluid-rock interactions: a case study from the Eastern Moldanubicum (Bohemian Massif). J Geochem Explor 243:107111. https://doi.org/10.1016/j.gexplo.2022.107111

Wolf MB, London D (1994) Apatite dissolution into peraluminous haplogranitic melts: an experimental study of solubilities and mechanisms. Geochim Cosmochim Acta 58:4127–4145. https://doi.org/10.1016/0016-7037(94)90269-0

Wu B, Bonnetti C, Liu Y, Zhang ZS, Guo GL, Li GL, Hu YQ, Yan ZY (2021) Uraninite from the Guangshigou pegmatite-type uranium deposit in the North Qinling Orogen, Central China: its occurrence, alteration and implications for post-Caledonian uranium circulation. Minerals 11:729. https://doi.org/10.3390/min11070729

Xie L, Wang RC, Chen J, Zhu JC (2010) Mineralogical evidence for magmatic and hydrothermal processes in the Qitianling oxidized tin-bearing granite (Hunan, South China): EMP and (MC)-LA-ICPMS investigations of three types of titanite. Chem Geol 276:53–68. https://doi.org/10.1016/j.chemgeo.2010.05.020

Xing Y, Etschmann B, Liu W, Mei Y, Shvarov Y, Testemale D, Tomkins A, Brugger J (2019) The role of fluorine in hydrothermal mobilization and transportation of Fe, U and REE and the formation of IOCG deposits. Chem Geol 504:158–176. https://doi.org/10.1016/j.chemgeo.2018.11.008

Yang WB, Niu HC, Shan Q, Sun WD, Zhang H, Li NB, Jiang YH, Yu XY (2014) Geochemistry of magmatic and hydrothermal zircon from the highly evolved Baerzhe alkaline granite: implications for Zr–REE–Nb mineralization. Miner Deposita 49:451–470. https://doi.org/10.1007/s00126-013-0504-1

Žák J, Verner K, Janoušek V, Holub FV, Kachlík V, Finger F, Hajná J, Tomek F, Vondrovic L, Trubač J (2014) A plate-kinematic model for the assembly of the Bohemian Massif constrained by structural relationships around granitoid plutons. Geol Soc Spec Publ 405:169–196. https://doi.org/10.1144/SP405.9

Zaraisky GP, Korzhinskaya V, Kotova N (2010) Experimental studies of Ta_2O_5 and columbite–tantalite solubility in fluoride solutions from 300 to 550 °C and 50 to 100 MPa. Miner Petrol 99:287–300. https://doi.org/10.1007/s00710-010-0112-z

Zeng Z, Liu Y (2022) Magmatic–hydrothermal zircons in syenite: a record of Nb–Ta mineralization processes in the Emeishan large igneous province. SW China Chem Geol 589:120675. https://doi.org/10.1016/j.chemgeo.2021.120675

Zhang L, Li X, Wang G, Wang M (2020) Direct evidence for the source of uranium in the Baiyanghe deposit from accessory mineral alteration in the Yangzhuang granite porphyry, Xinjiang Province, northwest China. Am Mineral 105:1556–1571. https://doi.org/10.2138/am-2020-7383

Zhang L, Wang F, Zhou T, Chen Z, Du X, Zhang S (2022) The origin of uranium deposits related to the Huangmeijian A-type granite from the Lu-Zong volcanic basin, South China: constraints from zircon U-Pb geochronology and mineral chemistry. Ore Geol Rev 141:104665. https://doi.org/10.1016/j.oregeorev.2021.104665

Zhang L, Wang F, Zhou T, Chen Z (2023) Contrasting alteration textures and geochemistry of allanite from uranium-fertile and barren granites: insights into granite-related U and ion-adsorption REE mineralization. Am Mineral 108:1298–1314. https://doi.org/10.2138/am-2022-8531

Zhong S, Feng C, Seltmann R, Li D, Qu H (2018) Can magmatic zircon be distinguished from hydrothermal zircon by trace element composition? The effect of mineral inclusions on zircon trace element composition. Lithos 314:646–657. https://doi.org/10.1016/j.lithos.2018.06.029